Differential growth and transcriptomic profile of stem cell-derived midbrain astrocytes

Zongze Li[1&2], Lucia Fernandez Cardo[1], Michal Rokicki[1], Jimena Monzón-Sandoval[1], Viola Volpato[1], Frank Wessely[1], Caleb Webber[1*], Meng 89Li[2*]

[1] Dementia Research Institute, School of Medicine, Cardiff University, Hadyn Ellis Building, Maindy Road, Cardiff, CF24 4HQ, UK

[2] Neuroscience and Mental Health Innovation Institute, School of Medicine, Cardiff University, Hadyn Ellis Building, Maindy Road, Cardiff, CF24 4HQ, UK

*Corresponding authors:

Meng Li, lim26@cardiff.ac.uk,

Caleb Webber, webberc4@cardiff.ac.uk

Key words: astrocyte, regional heterogeneity, ventral midbrain, dopaminergic, single cell RNA-sequencing

Abstract

Regional specificity of stem cell-derived astrocytes is believed to be an important prerequisite for their applications in disease modelling and cell-based therapies. The regional identity of these astrocytes is often defined by the positional characteristics of their antecedent, stem cell-derived neural progenitors patterned to a fate of interest, with the assumption that the positional specification is to be preserved by the derived astrocytes. Using a human induced pluripotent stem cell line designed for tracing midbrain floor plate derivatives, here we show that lineage composition of the derived astrocytes is not a faithful recapitulation of the founder progenitor population, as demonstrated by the loss of floor plate differentiated progeny in the final astrocyte products. Using deep single cell RNA sequencing, we identified distinct transcriptomic signatures of midbrain floor plate-derived astrocytes. Our study highlights the need for rigorous characterisation of pluripotent stem cell-derived regional astrocytes and provides a valuable resource for assessing midbrain floor plate-derived human astrocytes.

Introduction

Astrocytes are the most abundant cells in the brain. They play important roles in the central nervous system in supporting neuronal survival and synaptic activities, including the regulation of ionic homeostasis, providing energetic support, elimination of oxidative stress, and neurotransmitter removal and recycle (Verkhratsky and Nedergaard 2018). Abnormalities in astrocytes have been linked to various neurodegenerative and neurodevelopmental disorders, such as Parkinson's disease, Alzheimer's disease, Huntington's disease, autism spectrum disorders and Alexander's disease (Molofsky et al. 2012; Phatnani and Maniatis 2015; Booth et al. 2017). There is therefore a growing interest in using human pluripotent stem cell (PSC)-derived astrocytes for disease modelling *in vitro* (Chandrasekaran et al. 2016).

Contrary to the widely held belief that astrocytes in the brain are largely identical, recent studies revealed diversity in their transcriptomic profile, physiological properties and function (Oberheim et al. 2009; Schober et al. 2022). For example, single cell and spatial transcriptomic studies have identified several astrocyte subpopulations in the mouse cortex (Zhu et al. 2018; Batiuk et al. 2020; Bayraktar et al. 2020). In human, although astrocyte heterogeneity remains largely elusive, heterogeneity in radial glia across brain regions and within midbrain has been reported (La Manno et al. 2016; Li et al. 2023). Furthermore, different molecular and physiological features and distinct responses to stimuli were also observed in astrocytes from different mouse brain regions (Takata and Hirase 2008; Chai et al. 2017; Morel et al. 2017; Itoh et al. 2018; Kostuk et al. 2019; Makarava et al. 2019; Xin et al. 2019; Lozzi et al. 2020). Indeed, astrocyte heterogeneity has been suggested to underly the regional susceptibility to human diseases (Schober et al. 2022). Therefore, recapitulating astrocyte regional specificity in PSC-derived astrocytes is generally accepted as an important prerequisite.

Several reports have described the generation of regional astrocytes from human embryonic stem cells or induced pluripotent stem cells (iPSCs) which include forebrain (Krencik et al. 2011; Zhou et al. 2016; Tcw et al. 2017; Lin et al. 2018; Bradley et al. 2019; Hedegaard et al. 2020; Peteri et al. 2021), ventral midbrain (Booth et al. 2019; Barbuti et al. 2020; Crompton et al. 2021; de Rus Jacquet et al. 2021), hindbrain and

spinal cord (Roybon et al. 2013; Serio et al. 2013; Holmqvist et al. 2015; Bradley et al. 2019; di Domenico et al. 2019; Yun et al. 2019). The regional identity of these astrocytes is typically evaluated at the stage of early neural progenitors generated via cell type- or region-directed neural patterning protocols, with the assumption that the positional characteristics will be faithfully preserved in the final astrocyte products. However, astrocyte production in vitro involves an extended period of astrocytic fate induction and progenitor expansion using FGF and EGF while substantial literature reported alterations in region-specific gene expression and/or neurogenic competence in expanded neural progenitors (Jain et al. 2003; Sun et al. 2008; Koch et al. 2009; Falk et al. 2012). Therefore, better characterisations of PSC-derived astrocytes and their lineage-specific features are needed to advance our knowledge about the molecular heterogeneity of human astrocytes.

Using a human iPSC line that allows the tracing of LMX1A expressing midbrain floor plate neural progenitors and their differentiated progeny (Cardo et al. 2023), we discovered an unexpected gradual depletion of LMX1A$^+$ progenitor progeny during astrocyte induction from a bulk population of ventral midbrain patterned progenitors despite LMX1A$^+$ progenitors being the predominant starting population. LMX1A$^+$ progenitor derived astrocytes can however be generated if astrocytic induction is initiated from purified LMX1A$^+$ progenitors, indicating that the positional constituents of the founding cell population may not be preserved faithfully in the derived astrocytes. Single cell RNA sequencing (scRNAseq) of astrocytes derived from both parental populations identified distinct transcriptomic signatures, providing a useful resource for assessment of human PSC-derived midbrain astrocytes.

Results

Depletion of LMX1A$^+$ progenitors and/or derivatives in ventral midbrain patterned neural progenitor cultures during astrogenic induction

To investigate whether regionally patterned neural progenitors retain their lineage identity during astrogenic induction and glial progenitor expansion, we made use of

the LMX1A-Cre/AAVS1-BFP iPSCs tracer line, which enables the tracking of LMX1A$^+$ midbrain floor plate progenitors and their differentiated progeny(Cardo et al. 2023). We differentiated the LMX1A-Cre/AAVS1-BFP iPSCs towards the ventral midbrain fate following a modified protocol based on Jaeger *et al.* and Nolbrant *et al.*(Jaeger et al. 2011; Nolbrant et al. 2017)(Figure 1A). Immunocytochemistry of day (d)19 cultures confirmed a high proportion of cells expressing BFP (96.01±0.42%) and ventral midbrain progenitor markers LMX1A (92.94±0.91%), FOXA2 (94.76±0.57%) and OTX2 (97.82±0.28%; Figure 1B-D with the original images shown in Figure S1A). Most cells (91.26±1.64%) co-expressed LMX1A and FOXA2 (Figure 1B and 1D). At this stage, all BFP$^+$ cells also stained positive to a pan neural progenitor marker NESTIN (Figure 1C). We detected a small proportion of cells expressing midbrain basal plate marker NKX6.1 (2.03±0.47%, Figure 1B-C) whose expression domain in the early developing ventral midbrain partially overlap with that of (Andersson et al. 2006)(Andersson et al. 2006). However, few PAX6$^+$ cells were present (Figure 1C), which marks the forebrain and (Duan et al. 2013)(Duan et al. 2013). Immunocytochemical analysis of FACS-sorted BFP$^+$ cells confirmed highly enriched expression of LMX1A (95.51±0.09%) and FOXA2 (95.35±0.14%), and co-expression of both markers (94.68±0.10%; Figure 1B and 1D). In contrast, only a small number of LMX1A$^+$ cells (4.96±0.70%) were present in the sorted BFP$^-$ population (Figure 1B and1D). These findings provide further support that BFP expression faithfully recapitulate LMX1A expression and that LMX1A$^+$ ventral midbrain progenitors represent the major cell population in d19(Cardo et al. 2023)(Cardo et al. 2023).

The d19 cells were then induced to undergo astrogenic switch in media containing FGF2 and EGF with the BFP content monitored by flow cytometry at each weekly passaging (Figure 1A, representative gating strategy is shown in Figure S1B-E). We found, unexpectedly, a dramatic decrease of BFP$^+$ cell proportion from the starting point of 88.20±1.10% to only 27.59±8.28% at d43 and to nearly absent as the differentiation continued (Figure 1E). We did not observe evident cell death during culture and replating; thus, the absence of BFP could be either due to the silencing of BFP expression in the derivatives of LMX1A$^+$ progenitors or the loss of these cells through growth competition. To address this question, we performed progenitor expansion and astrogenic induction under the same culture condition with purified d19

BFP$^+$ progenitors isolated using fluorescence-activated cell sorting (FACS). Interestingly, the sorted BFP$^+$ cells exhibited similar population growth rate to that of unsorted cultures, and the proportion of BFP$^+$ cells remained at approximately 90% throughout the astrogenic induction and glial progenitor expansion period (Figure 1E). This observation demonstrates that BFP expression can be maintained in the derivatives of LMX1A$^+$ midbrain floorplate progenitors, and that the loss of BFP$^+$ cells in the unsorted culture is likely due to their growth disadvantage compared to the derivatives of LMX1A$^-$ progenitors.

Our finding is unexpected and demonstrates that the regional or lineage identity of PSC-derived astrocytic cells should not be assumed merely based on the dominant regional property of their cellular origin, given that no *in vitro* fate specification paradigm is 100% efficient.

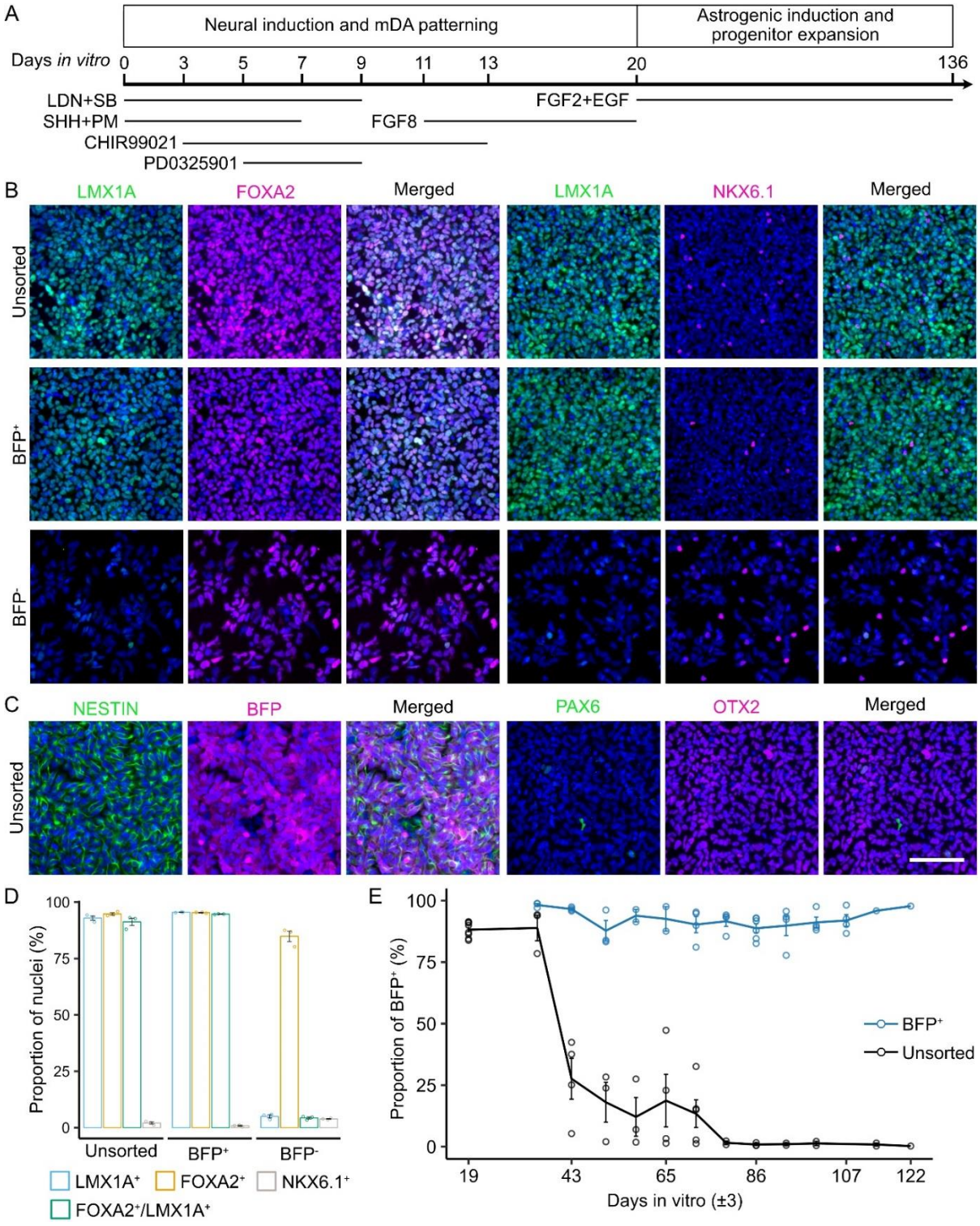

Figure 1. Depletion of LMX1A$^+$ progenitors and their derivatives during astrogenic induction in ventral midbrain patterned neural progenitor cultures.

A, Schematic diagram of ventral midbrain neural differentiation and astrogenic induction. B-C, Representative view of immunocytochemistry of ventral midbrain neural progenitor markers and other regional markers in d19 unsorted, sorted BFP$^+$, and sorted BFP$^-$ population. Scale bar represents 100 μm. Images shown were cropped to 300 μm × 300 μm by randomly selecting the region of interest in the nuclei-

only channel (uncropped greyscale images are shown in Figure S1A). D, Quantification of marker expression in unsorted, sorted BFP$^+$, and sorted BFP$^-$ population. Error bars represent the standard error of means (SEM) of three independent experiments. E, Flow cytometry quantification of unsorted and BFP+ population during astrogenic induction and progenitor expansion. Each data point represents one biological replicate. The gating strategy used is shown in Figure S1B.

Astrogenic switch occurred earlier in derivatives of LMX1A$^+$ midbrain progenitors.

Since sorted BFP$^+$ (LMX1A$^+$ or their derivatives) and unsorted astrocytic cultures differ distinctively in BFP expression soon after the initiation of astrogenic induction, for simplicity, these cultures are hereafter referred to as the BFP$^+$ and BFP$^-$ cultures, respectively. Wondering whether the two cell populations behave differently in the process of astrogenic switch, we examined astrocytic marker expression in these cultures at d45 and d98 by immunocytochemistry. SOX9 and NFIA are transcription factors crucial for the initiation of astrogenesis and acquisition of astrogenic competence in the developing central nervous system (Stolt et al. 2003; Deneen et al. 2006), while CD44 identifies astrocyte-restricted precursors (Liu et al. 2004). We found that all these markers were more abundantly detected in the BFP$^+$ cultures (NFIA: 65.89±2.81%; SOX9: 57.19±4.25%) than the BFP$^-$ cultures (NFIA: 4.26±1.28%; SOX9: 8.88±1.82%) at d45 (Two-way ANOVA with post-hoc Turkey test, NFIA: $p=2.52\times10^{-5}$, SOX9: $p=9.21\times10^{-6}$; Figure 2A-B with the original images shown in Figure S2). Although the number of NFIA$^+$ and SOX9$^+$ cells significantly increased in the BFP$^-$ cultures by d98 (NFIA: 44.07±4.56% on d98, $p=3.58\times10^{-4}$; SOX9: 44.28±2.84% on d98, $p=1.21\times10^{-4}$), the BFP$^+$ cultures still contained more cells expressing NFIA (65.71±4.25%; $p=2.06\times10^{-2}$) and SOX9 (73.25±2.12%; $p=5.51\times10^{-4}$) than BFP$^-$ cultures (Figure 2A and 2C).

To investigate whether the temporal difference in astrocytic switch between the BFP$^+$ and BFP$^-$ cultures affects maturation and functionality of the derived astrocytes, we initiated astrocyte terminal differentiation by exposing the BFP$^+$ and BFP$^-$ astrocyte precursors to CNTF and BMP4 (Krencik et al. 2011; Bradley et al. 2019) from d87 (referred to as early astrocytes) and d136 (late astrocytes). Both BFP$^+$ and BFP$^-$

cultures exhibited a similar expression profile of classic astrocyte markers, including AQP4, EAAT2, and S100B, but few $GFAP^+$ cells at both time points (Figure 2B and 2D with the original images shown in Figure S3).

As a reference, we also generated neural progenitors without employing any patterning cues and induced astrogenic switch and astrocyte differentiation from these non-patterned neural progenitors (Figure S4A-B). We found that, while the astrocyte cultures derived from the non-patterned progenitors contained a similar proportion of cells expressing AQP4, EAAT2 and S100B compared to the BFP^+ and BFP^- astrocyte cultures, there are more $GFAP^+$ cells in the non-patterned astrocyte preparations (17.89±5.4%, Figure S4A-B).

Functional astrocytes exhibit transient calcium (Ca^{2+}) spikes upon chemical stimulation, such as ATP (Zhang et al. 2016). Using a FLIPR Ca^{2+} release assay, we observed a sharp increase in the intracellular Ca^{2+} concentration upon ATP administration in both the early and late BFP^+ astrocyte populations (early BFP^+: $p=5.37\times10^{-12}$; late BFP^+: $p<2.2\times10^{-16}$; Figure 2E-F). ATP induced $Ca2^+$ release is partially mediated by inositol trisphosphate. Indeed, addition of an inositol trisphosphate receptor antagonist 2-aminoethoxydiphenylborate (2-APB) reduced the amplitude (early BFP^+: $p=5.88\times10^{-5}$; late BFP^+: $p=9.22\times10^{-10}$; Figure 2F) and rise time (early BFP^+: $p=2.63\times10^{-5}$; late BFP^+: $p=3.59\times10^{-4}$; late BFP^-: p=0.028; Figure 2G) of ATP-induced $Ca2^+$ response in both the early and late BFP^+ astrocytes. Interestingly, the early BFP^+ astrocytes had significantly lower peak amplitude than that observed in late BFP^+ astrocytes ($p=6.92\times10^{-9}$; Figure 2F), despite their similar level of astrocyte marker expression, suggesting a difference in maturity at the functional level. Early and late BFP^- astrocytes exhibited a similar profile of time-dependent increase in the amplitude of ATP-induced Ca^{2+} response but did not reach statistical significance (Figure 2E-F). However, late BFP^- astrocytes showed a significantly lower peak amplitude than late BFP^+ astrocytes ($p<2.2\times10^{-16}$; Figure 2E-F).

Taken together, our data demonstrate that astrogenesis occurred earlier in BFP^+ cultures than BFP^- cells. This temporal difference is also reflected in functional maturity of the derived astrocytes, despite a similar expression profile of classic astroglial markers.

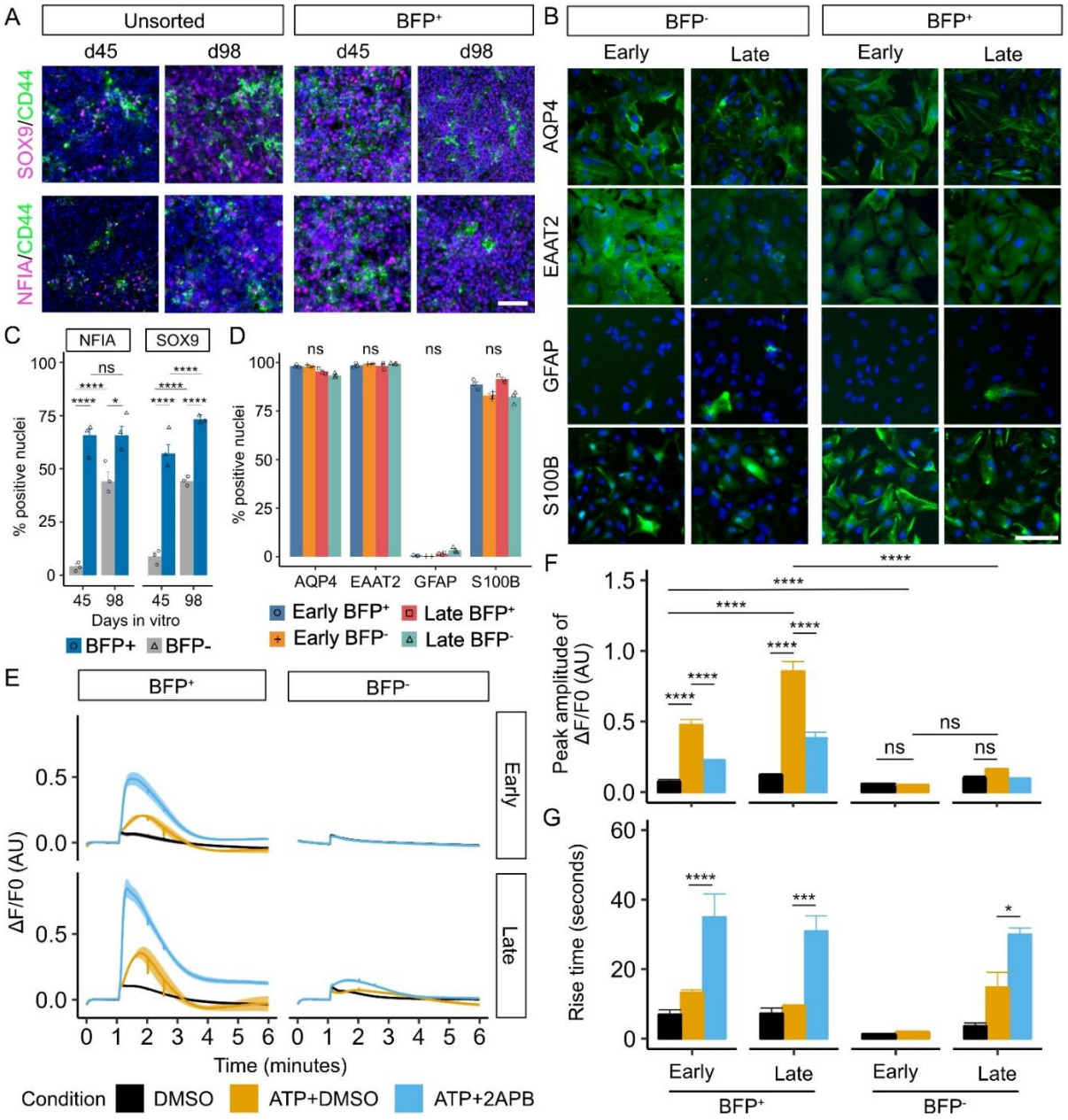

Figure 2. Early astrogenic switch and astrocyte maturation in derivatives of LMX1A$^+$ midbrain progenitors.

A, Representative view of immunocytochemistry of astrogenic marker expression in BFP$^+$ and unsorted progenitors at day 45 and 98. Scale bar represents 100 µm. Images shown were cropped to 462 µm × 462 µm by randomly selecting the region of interest in the nuclei-only channel (uncropped greyscale images are shown in Figure S2). B, Representative view of immunocytochemistry of astrocyte marker expression in early and late, BFP$^+$ and BFP$^-$ (unsorted) astrocytes. Scale bar represents 100 µm. Images shown were cropped to 300 µm × 300 µm by randomly selecting the region of interest in the nuclei-only channel (uncropped greyscale images are shown in Figure S3). C, Quantification of immunocytochemistry of astrogenic marker in BFP$^+$ and BFP$^-$ progenitors at day 45 and 98 shown in Panel A. Error bars represent the standard error of means (SEM) of three independent experiments. Two-way ANOVA was

performed to compare between lineages (NFIA: $p=5.389\times10^{-6}$, df=1, effect size=3.62; SOX9: $p=1.96\times10^{-6}$, df=1, effect size=4.77) and days of differentiation (NFIA: $p=7.82\times10^{-5}$, df=1, effect size=1.99; SOX9: $p=2.62\times10^{-5}$, df=1, effect size=2.99) D, Quantification of immunocytochemistry of astrocyte marker expression in astrocytes. Error bars represent SEM of three independent experiments. Kruskal-Wallis test results following Bonferroni correction are shown on the top of the figure (AQP4: p.adjust=0.12, df=3, H=8.95; EAAT2: p.adjust=1.00, df=3, H=0.95; GFAP: p.adjust=0.06, df=3, H=10.38; S100B: p.adjust=0.11, df=3, H=9.05). E, Averaged trace of ATP-induced Ca^{2+} response assayed using FLIPR. Drugs or DMSO were applied at 1 minute of the assay. The line represents the average fluorescence change (ΔF/F0) in at least three independent experiments each with at least three replicate wells. The shaded area represents the SEM across at least three independent experiments. F, Quantitative comparison of the peak amplitude of ATP-induced Ca^{2+} response among conditions (two-way ANOVA, $p<2.2\times10^{-16}$, df=2, effect size=2.54) and samples ($p=2.87\times10^{-14}$, df=3, effect size=2.17). Error bars represent the SEM across at least independent experiments. G: Quantitative comparison of the rise time of ATP-induced Ca^{2+} response among conditions (two-way ANOVA, $p=2.19\times10^{-13}$, df=2, effect size =1.958) and samples (p=0.064, df=3, effect size=0.76). Intergroup comparison was performed using Post-hoc Tukey test. Error bars represent the SEM across at least three independent experiments. (****: p<0.0001, ***: p<0.001, **: p<0.01, *: p<0.05, ns: not significant).

Single cell RNA sequencing confirms the authenticity of PSC-derived astrocytes.

To further characterize the PSC-derived astrocytes, we performed full-length scRNAseq on early and late BFP^+ and BFP^- astrocytes using the iCELL8 platform and SMART-seq technology, with non-patterned astrocytes derived from the LMX1A-Cre/AAVS1-BFP tracer line as a control. A sample of iPSC-derived neurons was included to facilitate downstream cell type identification. We profiled FACS purified astrocytes expressing CD49f as well as unsorted cultures for comparison of all three astrocyte populations (Barbar et al. 2020); Figure S4C-H). After stringent filtering (Figure S5A-C, see Methods and Materials on filtering), we obtained a total of 17478 protein-coding genes in 1786 qualifying cells, with an average of 6326 protein-coding genes detected per cell.

Unsupervised Louvain clustering identified 12 cell clusters (Figure 3A). Cells clustered mainly based on sample type (astrocytes and neurons; Figure S6A) and the estimated cell cycle phase (Figure S6B), while sorted $CD49f^+$ and unsorted astrocytes were

clustered together (Figure S6A). *TagBFP* was detected at a higher level in BFP^+ astrocyte samples than in BFP^- and NP samples, while *TagBFP* expression was negligible in the neuronal samples derived from an iPSC line without BFP transgene (Figure S6C-D). Using a set of known astrocyte and neuronal signature genes (Figure 3B), we identified cells in clusters 0, 1, and 5-11 as astrocytes (Figure 3B), which were enriched in expression of *SOX9*, *NFIA*, *NFIB*, *HES1*, *S100A13*, *S100A16*, *EGFR*, *CD44* and *GJA1* (Figure 3B). These transcripts were also detected at high levels in clusters 2 and 4, which were mostly estimated to be in cell cycle phases G2, M and S (Figure S6B). In addition, clusters 2 and 4 showed high levels of proliferation-related transcripts, such as *TOP2A, MKI67, CDK1* and *AURKA* (Figure 3B), and are thus defined as astrocyte precursors. In contrast, Cluster 3 contains mostly cells from the neuronal sample (Figure 3A and Figure S6A) and indeed expressed high levels of genes closely related to neuronal structure and function (such as *STMN2*, *SYT1*, *DCX*, *MAPT*, and *SNAP25*; Figure 3B). We did not detect transcripts indicative of endoderm (*GATA4*), mesoderm (*TBXT* and *TBX6*), and oligodendrocyte progenitors (*SOX10* and *PDGFRA*) in any of these clusters (Figure S6C).

To determine the authenticity of these PSC-derived astrocytes, we mapped our data to published scRNAseq datasets obtained from five foetal, an adult human brain and a PSC-derived astrocyte study using Seurat integration (La Manno et al. 2016; Sloan et al. 2017; Zhong et al. 2018; Polioudakis et al. 2019; Agarwal et al. 2020; Fan et al. 2020; Bhaduri et al. 2021; Eze et al. 2021). We found that cells in clusters annotated as astrocytes (clusters 0, 1, and 5-11) were indeed predominantly mapped to the reference astrocyte or astrocyte precursor populations with high confidence (prediction score over 0.5; Figure 3C and Figure S7). In contrast, neuronal cluster 2 was mapped to neurons of the foetal reference datasets, while the astrocyte precursor clusters (2 and 4) were mapped to progenitor populations in the foetal reference datasets (Figure 3C and Figure S7). These findings demonstrate that our iPSC-derived astrocytes closely resemble those in the human brains.

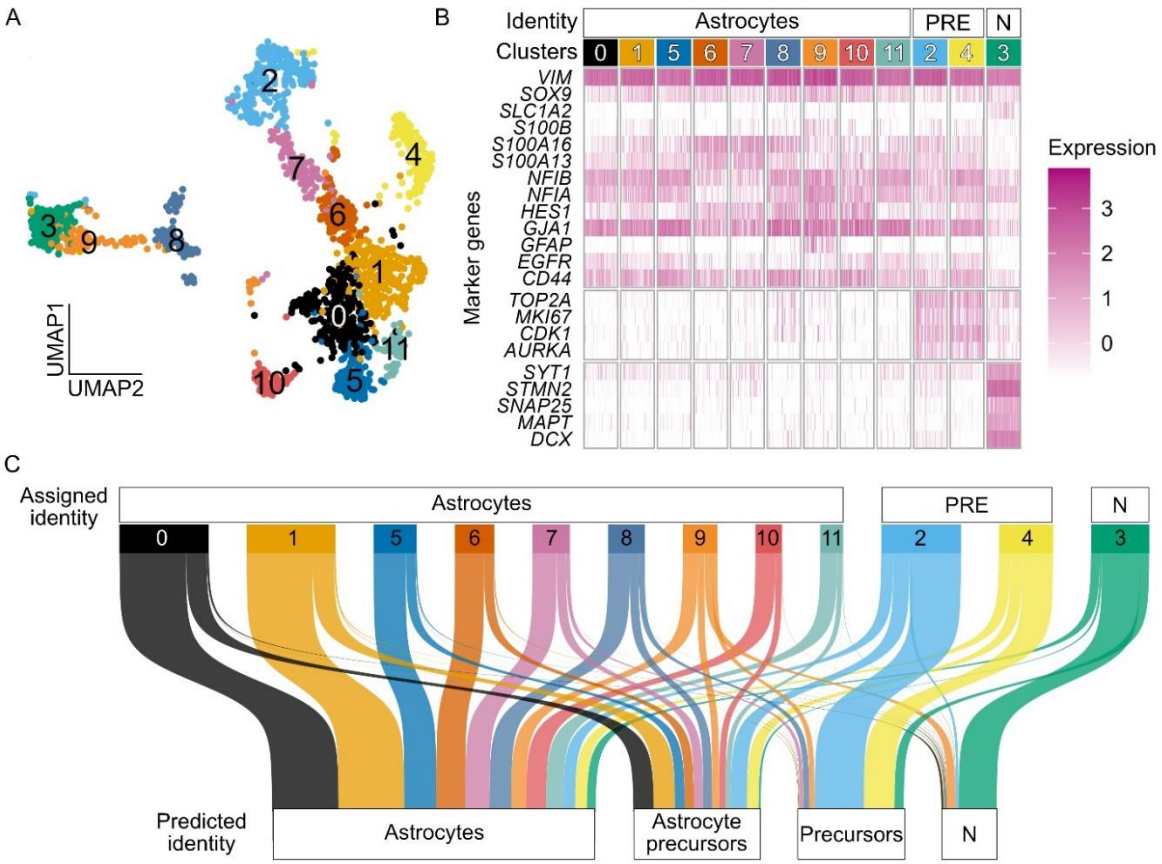

Figure 3. Single cell RNA sequencing confirms the authenticity of PSC-derived astrocytes.

A, Uniform manifold approximation and projection plot of unbiased clustering, coloured by clusters. B, Heatmap of the normalised expression of selected markers in different clusters. The assigned identity to each cluster is shown at the top of the plot. C, Sankey plot summarising the result of reference mapping of cells in different clusters to eight published reference human brain scRNAseq datasets. The thickness of the thread is proportional to the number of cells mapped to the same identity in the reference datasets (predicted identity). Detailed results of referencing mapping to each reference datasets are shown in Figure S7A-H and prediction score shown in Figure S7I. (PRE: precursors; N: neurons)

Distinct transcriptome fingerprints of LMX1A$^+$ midbrain floor plate-derived astrocytes

Significant advance has been made recently in understanding the molecular profiles of midbrain dopamine neurons. However, our knowledge about midbrain astrocytes in this regard remains limited and does not inform anatomic or lineage origin of the cells.

In this regard, the BFP$^+$ astrocytes provide a unique resource to determine the transcriptomic characteristics of human midbrain floor plate derived astrocytes. By performing pairwise differential gene expression (details described in Methods and Materials), we identified 1153 genes differentially expressed (DEGs; adjusted p values less than 0.05 and log2 fold change over 0.25) in BFP$^+$ astrocytes when compared to either BFP$^-$ or non-patterned astrocyte populations (Supplementary Data 1). Of these, 159 were unique to BFP$^+$ astrocytes (BFP$^+$ enriched, Figure 4A), which include genes associated with midbrain dopamine neuron development such as *SULF1*, *LMO3*, *NELL2*, and *RCAN2* (Figure 4B) (Strelau et al. 2000; La Manno et al. 2016; Bifsha et al. 2017; Ahmed et al. 2021). Interestingly, *LMX1A* and *FOXA2*, which was used to evaluate PSC-derived midbrain astrocytes in previous studies, were not detected in BFP$^+$ astrocytes (Figure S6D). We also identified 530 DEGs enriched in BFP$^-$ astrocytes only (BFP$^-$ enriched, Figure 4A and Supplementary Data 1), which include those known to be expressed in the ventrolateral - dorsal domain of the midbrain and hindbrain, such as *IRX3*, *IRX5*, *PAX3*, and *PAX7* (Figure 4B)(Houweling et al. 2001; Matsunaga et al. 2001). This transcription profile supports the notion that the BFP$^-$ astrocytes are descendants of the initial minor populations of lateral midbrain progenitors. Moreover, 72 DEGs were shared by BFP$^+$ and BFP$^-$ astrocytes against the non-patterned astrocytes (midbrain enriched, Figure 4A and Supplementary Data 1). This set of genes includes *NR2F1*, *NR2F2, ZEB2, KCNJ6* and *SRPX* (Figure 4B), which have been reported to be signatures of mouse midbrain astrocytes (Endo et al. 2022). Together, our findings provide a new entry to transcriptomic characteristics of midbrain astrocytes and specifically a gene expression map of midbrain floor plate derived human astrocyte lineage.

Gene ontology (GO) enrichment analysis was performed on the 1153 DEGs enriched in BFP$^+$ astrocytes (Supplementary Data 2). The significantly enriched GO terms were mainly related to various aspects of metabolism, stress response, biosynthesis, lysosomal activity, and cellular respiration (Figure 4C and Supplementary Data 3). These biological processes have previously been shown to be disrupted by several mutations causing familial Parkinson's disease (di Domenico et al. 2019; Barbuti et al. 2020; Sonninen et al. 2020). In contrast, the GO terms associated with 530 BFP$^-$ astrocyte enriched DEGs were mostly related to formation of extracellular matrix and

tissue development (Figure 4D and Supplementary Data 2-3). The differential enrichment of GO terms implicates functional difference between the BFP$^+$ and BFP$^-$ astrocytes and supports the need for generating regional specific astrocytes for disease modelling.

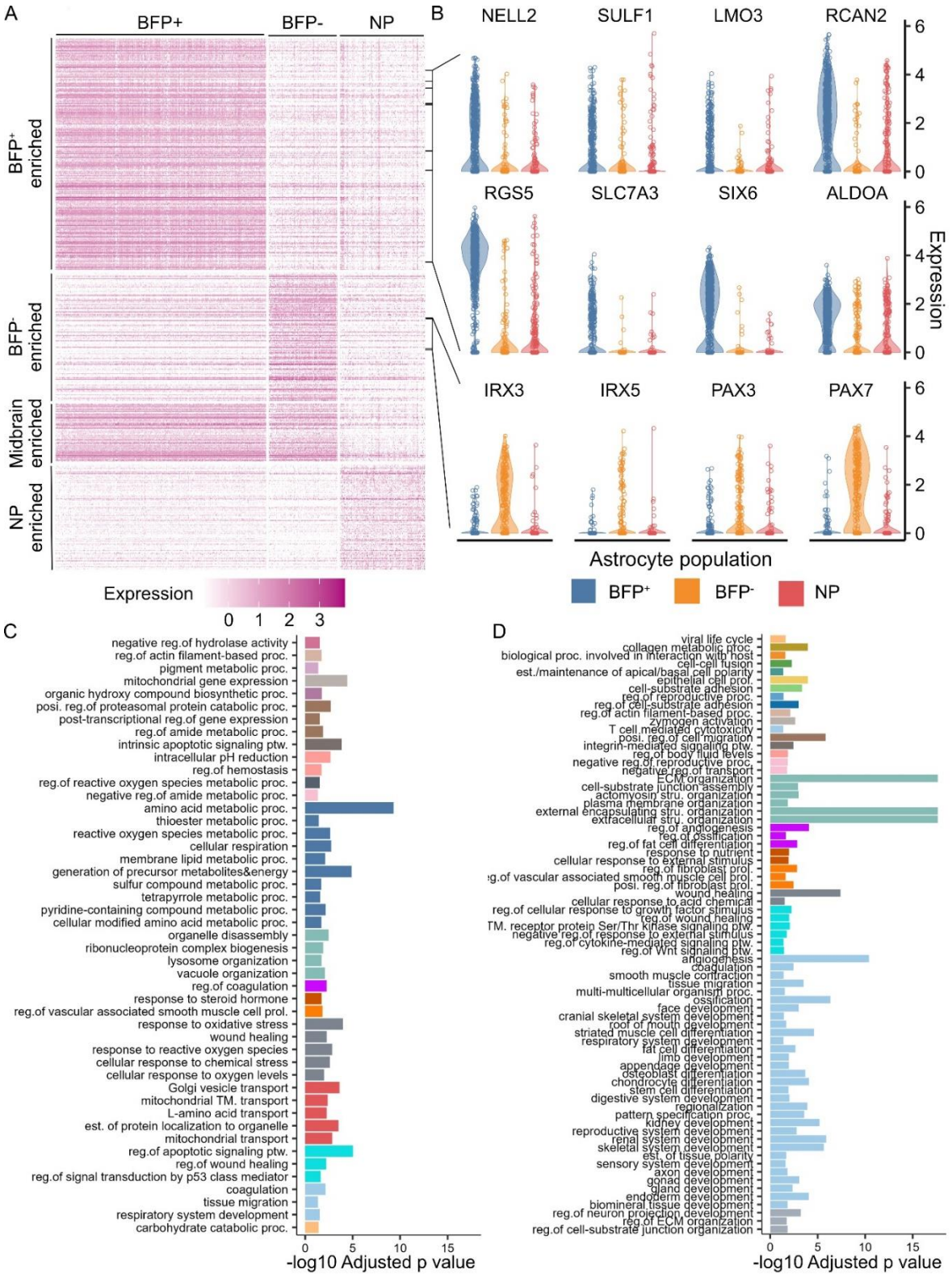

Figure 4. Distinct transcriptome fingerprints of LMX1A$^+$ midbrain floor plate-derived astrocytes

A, Heatmap of the normalised expression of population-specific genes in different populations of astrocytes. B, Violin plots of the normalised expression of selected candidate markers for BFP$^+$, BFP$^-$, and non-patterned (NP) astrocytes. C-D, Representative GO terms significantly enriched in BFP$^+$ (C) and BFP$^-$ (D) enriched genes. Semantically similar representative terms were shown with the same colour.

Discussion

Despite the general belief that recapitulating astrocyte lineage heterogeneity is necessary for stem cell-based disease modelling and cell transplantation, the extent of astrocyte heterogeneity in different brain regions and subregions remains largely elusive. By harnessing an LMX1A based lineage tracing human iPSC line and cutting edge scRNAseq technology, we show that astrocytes derived from the LMX1A$^+$ midbrain floor plate progenitors, the same cells giving rise to midbrain dopaminergic neurons, possess distinct transcriptional landmarks from those derived from non-midbrain patterned neural progenitors as well as other midbrain patterned progenitors. Moreover, we discovered unexpected negative selection against derivatives of LMX1A$^+$ progenitors during astrocyte induction and progenitor expansion. Our study highlights the need for careful characterisation of PSC-derived astrocytes and provides a transcriptomic fingerprint for midbrain floor plate derived astrocytes.

Using a popular astrocyte in vitro differentiation paradigm, we found that astrocytes descended from the LMX1A$^+$ midbrain progenitors could only be obtained from purified progenitors. In contrast, astrocytes derived from bulk midbrain patterned progenitors exhibits transcriptomic profiles of the lateral-dorsal midbrain, despite LMX1A$^+$ midbrain progenitors being the predominant starting population. Our findings demonstrate that the lineage composition of the parent progenitors may not be faithfully preserved during astrocyte induction and progenitor expansion. FGF is the most popular inductive molecule used for astrocyte differentiation from stem cells (Chandrasekaran et al. 2016). It is evident however that FGF expanded neural progenitors, originated either from the brain or neutralized PSCs, exhibit restricted regional competence and

371 positional gene expression. For example, bulk expanded human ventral midbrain
372 neural progenitors (Jain et al. 2003), and fetal forebrain or spinal cord derived neural
373 stem (NS) cells only give rise to GABAergic neurons (Sun et al. 2008); likewise, lt-
374 NES cells display anterior hindbrain-like positional profile (Falk et al. 2012), while their
375 antecedents, PSC-derived neural rosettes and early passage derivatives, express
376 anterior forebrain markers (Koch et al. 2009). It is not clear whether this is due to
377 deregulation of the original patterning at the level of gene expression or the loss of
378 associated cell population (Gabay et al. 2003). In this study, since BFP^+ astrocytes
379 can be generated under the same culture condition with purified $LMX1A^+$ progenitors,
380 we reasoned that the loss of their derivatives in unsorted cultures was possibly due to
381 differential growth capacity.

382 Our study highlights the need for careful assessment of astrocyte positional identity.
383 A common practice in this regard is to confirm the regional characteristics of the
384 founder progenitors following fate directed neural induction, with the assumption that
385 the dominant positional features will be maintained by the astrocyte progeny (Krencik
386 et al. 2011). This strategy is at least partly dictated by our limited knowledge in gene
387 expression signatures of regional- and/or lineage-specific astrocytes. Hence, an end
388 point evaluation of PSC-derived astrocytes often relies on region-specific markers
389 defined in the developmental brain during the neurogenic period. For example, LMX1A
390 and FOXA2 expression were used as criteria for midbrain astrocytes in previous
391 studies (Barbuti et al. 2020; Crompton et al. 2023). However, scRNAseq of human
392 fetal ventral midbrain and adult substantia nigra revealed negligible expression of
393 these transcripts in astrocytes (La Manno et al. 2016; Agarwal et al. 2020; Kamath et
394 al. 2022). Consistent with these findings, we did not detect LMX1A or FOXA2 in neither
395 the BFP^+ nor BFP^- astrocytes. Our analysis however identified new positive and
396 negative markers that could be applied to confirm the regional identity of ventral
397 midbrain astrocytes.

398 In addition to distinct transcriptomic profile, BFP^+ and BFP^- astrocytes may also be
399 functionally different. Astrocytes generated from progenitors broadly patterned to the
400 dorsal forebrain, ventral forebrain and spinal cord have been shown to exhibiting
401 different GO enrichment profile as well as different physiological and functional
402 properties (Bradley et al. 2019). In comparison to the BFP^- and non-patterned

astrocytes, the current study revealed that GO terms enriched in BFP^+ astrocytes, which originated from the same progenitor giving rise to midbrain dopaminergic neurons, were closely related to various biological processes disrupted in astrocytes carrying familial Parkinson's disease mutations (di Domenico et al. 2019; Barbuti et al. 2020; Sonninen et al. 2020). Such a distinct enrichment profile implicates BFP^+ astrocytes being functionally adapted to supporting midbrain dopaminergic neurons compared to BFP^- and non-patterned astrocytes.

In conclusion, this study lends further support on regional diversity of astrocytes and identified a set of midbrain enriched genes. Crucially, the transcriptomic fingerprint of human midbrain floor plate-derived astrocytes described here offers a much-needed resource for assessing the authenticity of stem cell derived astrocytes in studies associated with Parkinson's disease.

Methods and Materials

Stem cell culture and astrocyte differentiation

KOLF2 human iPSCs were maintained in E8 flex media (ThermoFisher) and manually dissociated using Gentle Cell Dissociation Reagent (STEMCELL Technologies) as previously described (Cardo et al. 2023). Astrocytes were differentiated using a three-stage stepwise strategy consisting neural induction and regional patterning, astrogenic switch and progenitor expansion, and astrocyte terminal differentiation. Midbrain floor plate progenitors were generated as previously described (Cardo et al. 2023). At day 19, cells were replated as single cells onto poly-D-lysine-laminin-coated plates at 1×10^6 cells/cm^2 for astrogenic switch and progenitor expansion in N2B27 media supplemented with 10 ng/mL FGF2 (Peprotech) and 10 ng/mL Human EGF (Peprotech) and replated every 6-8 days. For astrocyte terminal differentiation, expanded neural progenitors were re-plated at a density of 3×10^4 cells/cm^2 in expansion media and 24 hours later switched to N2B27 supplemented with 10 ng/mL human recombinant CNTF (Peprotech) and 10 ng/mL human recombinant BMP4 (Peprotech) for 7 days followed by media containing CNTF alone for another 13 days. 10 µM Y-27632 was used for 24 hours before and after each replating. The protocol

for generating non-patterned astrocytes was the same as for floor plate-derived astrocyte except the neural progenitors were derived with duo-SMAD inhibitors only without ventral patterning reagents.

Flow cytometry analysis and cell isolation

Cells were dissociated in Accutase as described above and washed twice with DPBS by centrifugation for 5 minutes at 200 rcf. For evaluating BFP expression, dissociated cells were resuspended in 0.5 mM EDTA in DPBS (Sigma-Aldrich) and analysed on a BD LSRFortessa cell analyser (BD Biosciences). For purifying BFP^+ cells, dissociated cells were resuspended in the same cell culture media. Background autofluorescence was compensated for using KOLF2 parental cell line at a similar stage of differentiation to define BFP^- gating. For purifying $CD49f^+$ astrocytes, dissociated cells were stained with Alexa Fluor 647-conjugated rat anti-CD49f antibody (5% v/v in a 100 µL reaction; BD Biosciences) for 25 minutes at 37°C on an orbital shaker at 200 rcf and resuspended in DPBS containing 0.5% bovine serum albumin and 50 units/mL DNase I (Sigma Aldrich). Background autofluorescence was compensated for using KOLF2 parental cell line at a similar stage of differentiation to define BFP^- gating and unstained astrocytes to define $CD49f^-$ gating. Cell sorting was performed on a BD FACSAria III (BD Biosciences) using an 80 µm nozzle. Sorted cells were collected in the same media as for resuspension. Flow cytometry data were analysed in FlowJo v10.8.1 (BD Biosciences) as shown in Figure S1B-E. Briefly, non-debris events were selected using the eclipse gates on dot graphs of SSC-A versus FSC-A. Singlet events were sequentially gated using polygonal gates on dot graphs of FSC-H versus FSC-A and SSC-H versus SSC-A by selecting the events in the diagonal region. The positive and negative gates in the fluorescence channel were set as bifurcate gates at a minimum of 99.9% percentile (usually at 99.99% percentile) on the histogram of the fluorescence intensity of the negative control sample of the same flow cytometry experiment and applied to all samples of the same flow cytometry experiment.

Immunocytochemistry

Cultures were fixed with 3.7% PFA for 15-20 min at 4 ºC. For nuclear antigen detection, an additional fixation with methanol gradient was performed, which include

5 mins each in 33% and 66% methanol at room temperature followed by 100% methanol for 20 min at -20°C. Cultures were then returned to PBST via inverse gradient and were then permeabilized with three 10-minute washes in 0.3% Triton-X-100 in PBS (PBS-T) and then blocked in PBS-T containing 1% BSA and 3% donkey serum. Cells were incubated with primary antibodies in blocking solution overnight at 4°C. Following three PBS-T washes, Alexa-Fluor secondary antibodies (Thermo Fisher Scientific) were added at 1:1000 PBS-T for 1 hour at ambient temperature in the dark. Three PBS-T washes were then performed that included once with DAPI (Molecular Probes). Images were taken on a Leica DMI6000B inverted microscope. Quantification was carried out in Cell Profiler (Stirling et al. 2021) or manually using ImageJ (Schindelin et al. 2012) by examining at least four randomly selected fields from three independent experiments. The antibodies used are provided in the Supplementary Table 1. Representative images shown in main figures were cropped by randomly selecting the region of interest in the DAPI-stained channel only, with the original unedited images shown in Figure S1A, S2 and S3.

Single-cell RNA-sequencing

Cells were dissociated with Accutase with 10 units/mL of papain (Sigma-Aldrich) for 10 minutes at 37°C and resuspended in 0.5% bovine serum albumin (Sigma Aldrich) with 50 units/mL DNase I in DPBS without calcium or magnesium (Gibco) and passed through a cell strainer with 35 µm mesh. Cells were stained with 1 µM SYTO16 (Invitrogen) and 0.08% (v/v) propidium iodide (part of the Invitrogen ReadyProbes™ Cell Viability Imaging Kit, Blue/Red) for 20 minutes on ice and then dispensed into the nano-well plates of the ICELL8® cx Single-Cell System (Takara). Wells containing single viable cells were automatically selected using the ICELL8 cx CellSelect v2.5 Software (Takara) with the green and not red logic. Manual triage was performed to recover additional candidate wells that contain viable single cells. The library for sequencing was then prepared using the SMART-Seq ICELL8 application kit (Takara) following the manufacturer's recommended protocol. Next-generation sequencing was performed using the NovaSeq6000 and the Xp Workflow on a S4 flow cell for 200 cycles of pair-end sequencing.

Single-cell RNA-sequencing analysis

Using the Cogent NGS Analysis Pipeline software v 1.5.1 (Takara), FASTQ files containing all indices for each chip were demultiplexed to FASTQ files containing one index per file. Adaptor sequences were removed using cutadapt 3.2 with the following settings: -m 15 --trim-n --max-n 0.7 -q 20. Trimmed FASTQ files were aligned to the *Homo sapiens* GRCh38.106 primary assembly with the BFP reporter gene attached to the end of the genome, using STAR 2.7.9a (Dobin et al. 2013) with the following settings: --outSAMtype BAM Unsorted --quantMode TranscriptomeSAM --outReadsUnmapped Fastx --outSAMstrandField intronMotif --chimSegmentMin 12 --chimJunctionOverhangMin 8 --chimOutJunctionFormat 1 --alignSJDBoverhangMin 10 --alignMatesGapMax 100000 --alignIntronMax 100000 --alignSJstitchMismatchNmax 5 -1 5 5 --chimMultimapScoreRange 3 --chimScoreJunctionNonGTAG -4 --chimMultimapNmax 20 --chimNonchimScoreDropMin 10 --peOverlapNbasesMin 12 --peOverlapMMp 0.1 –alignInsertionFlush Right --alignSplicedMateMapLminOverLmate 0 --alignSplicedMateMapLmin 30. After alignment, gene-level quantification was performed using featureCounts from subread 2.0.0 (Liao et al. 2013) with the following settings: -t exon --primary -R CORE -F GTF -Q 0 -B -g gene_id. The count matrix of each index was combined in R 4.2.0 (Team 2023).

All downstream analysis was performed in R 4.3.0 using Seurat 4.3.0 (Stuart et al. 2019). Gene-level filtering was applied by including only protein-coding genes with at least five total counts across all cells and being expressed in at least 1% of all cells. Poor quality cells were then identified using the *is.outlier* function from the scater 1.28.0 (McCarthy et al. 2017). Poor quality cells were defined as having a high percentage of mitochondrial gene count, or high or low the total number of genes detected, or high total gene counts. The thresholds of each metrics for each sample were determined as twice the median absolute deviation of the sample. Raw gene counts were log normalised with a scale.factor setting of 1×10^5. Data from the two batches of experiments were integrated using the *FindIntegrationAnchors* and *IntegrateData* based on the common top 2000 highly variable genes and the first 30 dimensions of principal components. The percentage of mitochondrial gene count and

total gene count were regressed out using the *ScaleData* function. Principal component analysis (PCA) was performed on the top 2000 high variable genes and the number of principal components used for uniform manifold approximation and projection (UMAP) was determined using the JackStraw method (Chung and Storey 2015). UMAP and unbiased Louvain clustering was performed on the first 33 principal components. Pairwise differential gene expression analysis was performed using the MAST method (Finak et al. 2015) with “Chip” as the latent variable. Gene ontology enrichment analysis was performed using *enrichGO* function in the clusterProfiler 4.10.0 package (Stirling et al. 2021) with all genes in the filtered dataset as the background. GO term database was downloaded using the org.Hs.eg.db 3.18.0 package (Carlson 2019). Revigo v1.8.1 was used to group the representative GO terms based on semantic similarity using a size setting of 0.5, Homo sapiens database, and SimRel method for semantic similarity (Schlicker et al. 2006; Supek et al. 2011).

Published datasets were downloaded from NCBI’s Gene Expression Omnibus (Clough and Barrett 2016) and processed in R 4.2.0. Gene level filtering was performed by retaining only protein-coding genes with more than five total counts across all cells. Gene counts were normalised using the NormalizeData function (scale.factor settings are listed in Supplementary Table 2). PCA was performed based on the top 2000 highly variable genes to obtain the first 50 PCs. Visual inspection of the elbow plot was used to determine the number of PCs for downstream analysis. Batch effect between subjects was evaluated on the two-dimensional PC2~PC1 plot. Where inter-subject batch effect was observed, Harmony integration was performed based on the PCs selected in the previous step (Supplementary Table 2). UMAP was performed based on either the PCA or Harmony reduction (using the top 30 dimensions), and Louvain clustering was performed (settings shown in Supplementary Table 2). Cluster identities were verified against the reported annotation where possible. For datasets without detailed annotation published or astrocyte lineage reported (Supplementary Table 2), reannotation was performed based on the expression of known markers (Figure S7A-E). Reference mapping was performed using *FindTransferAnchors* and *TransferData* function in Seurat based on the first 30 dimensions of either the PCA or Harmony loadings of the reference dataset.

Statistical analyses

All data were collected from at least three independent experiments and presented as mean ± standard error of means unless otherwise specified. Data were tested for normality with the Shapiro-Wilk test and for equal variance with Levene test before performing statistical analyses by two-way ANOVA with post-hoc Tukey test for multiple comparisons where relevant. Kruskal-Wallis test with post-hoc Dunn's test for pairwise comparison was used where parametric test was not suitable. Effect size was calculated as Cohen's f for ANOVA or eta squared based on the H-statistic for Kruskal-Wallis test. All statistical tests were performed in R4.3.0.

Supplementary Information

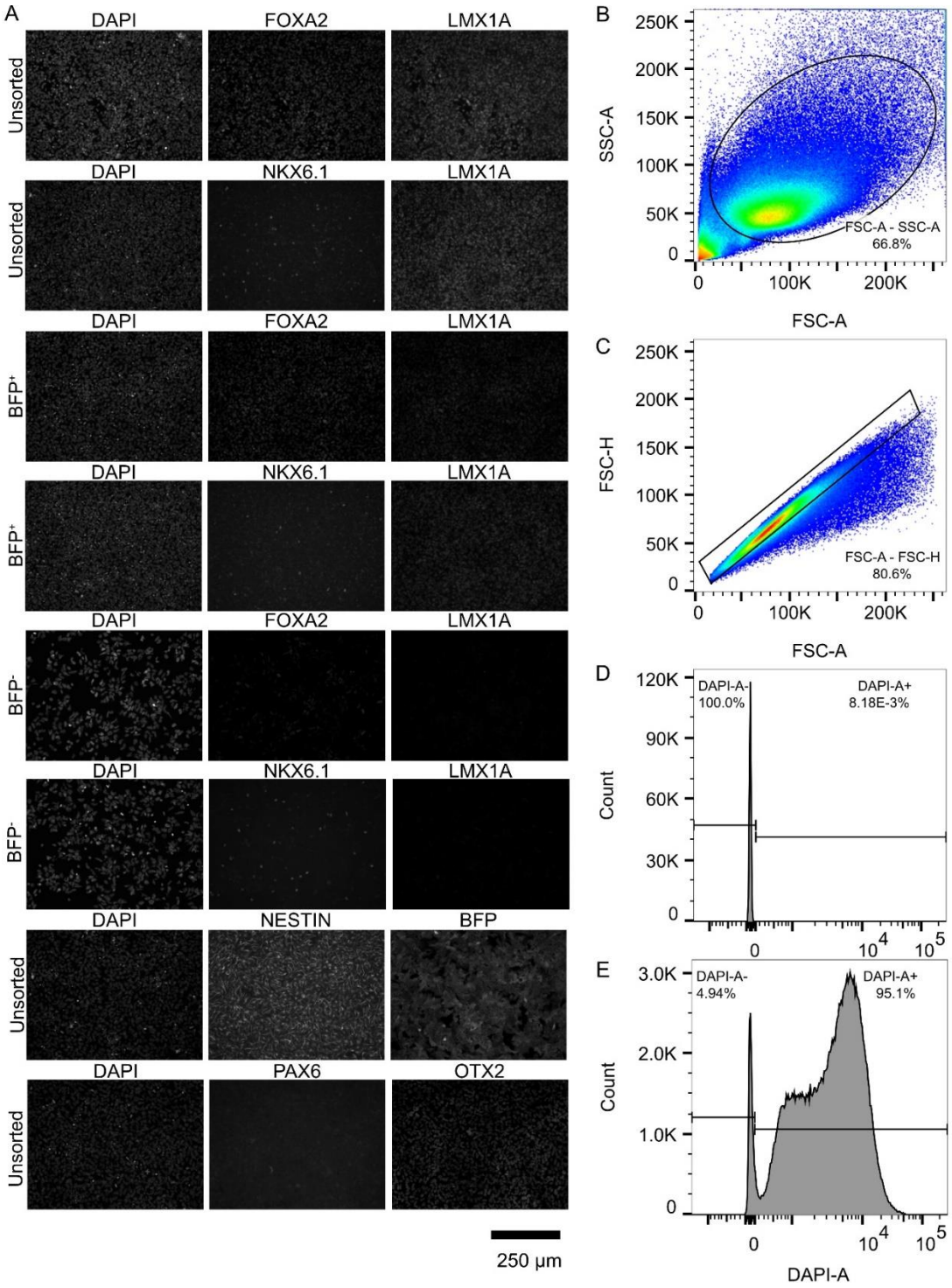

Figure S1. Original images of immunocytochemistry of d19 progenitors and gating strategy of BFP flow cytometry analysis.

A, the original images shown in Figure 1B-C. The gating strategy used for BFP flow cytometry analysis are shown in B-E and described in Methods and Materials. B,

570 scatter plot of SSC-A versus FSC-A. C, scatter plot of FSC-H versus FSC-A. D-E,
571 histogram of BFP fluorescence in the negative control (D) and BFP-expressing (E)
572 samples.
573

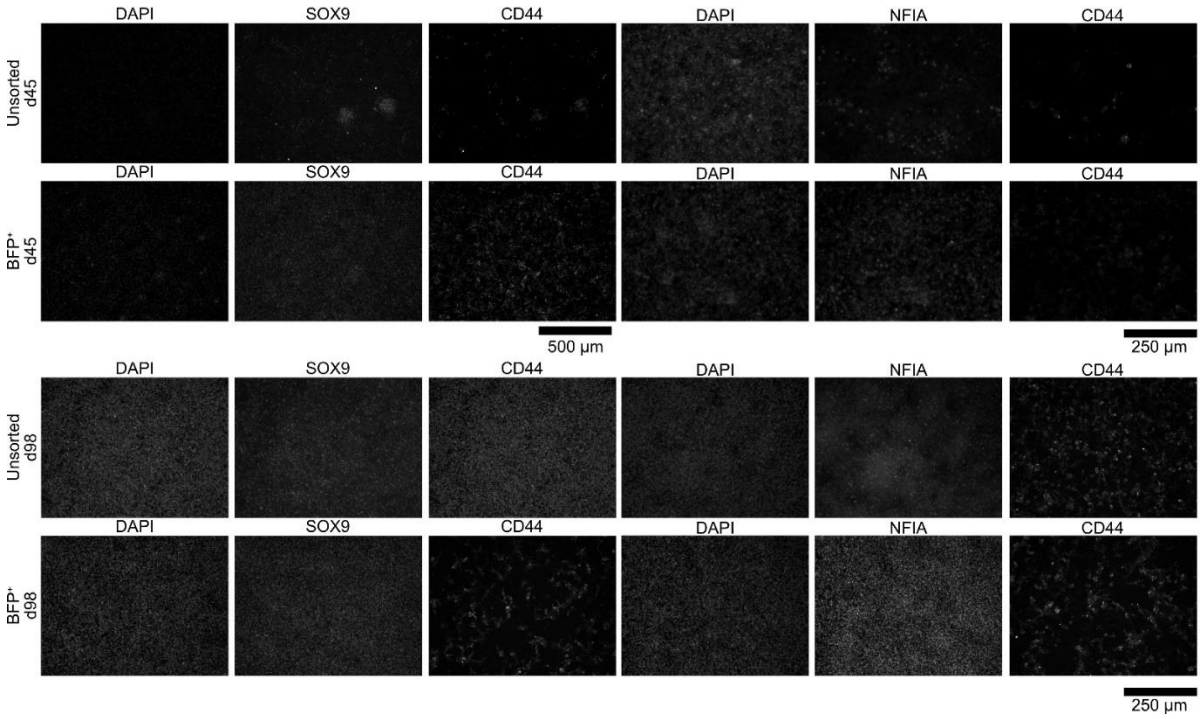

574
575 **Figure S2. Original images of immunocytochemistry of astrogenic markers**
576 **shown in Figure 2A.**

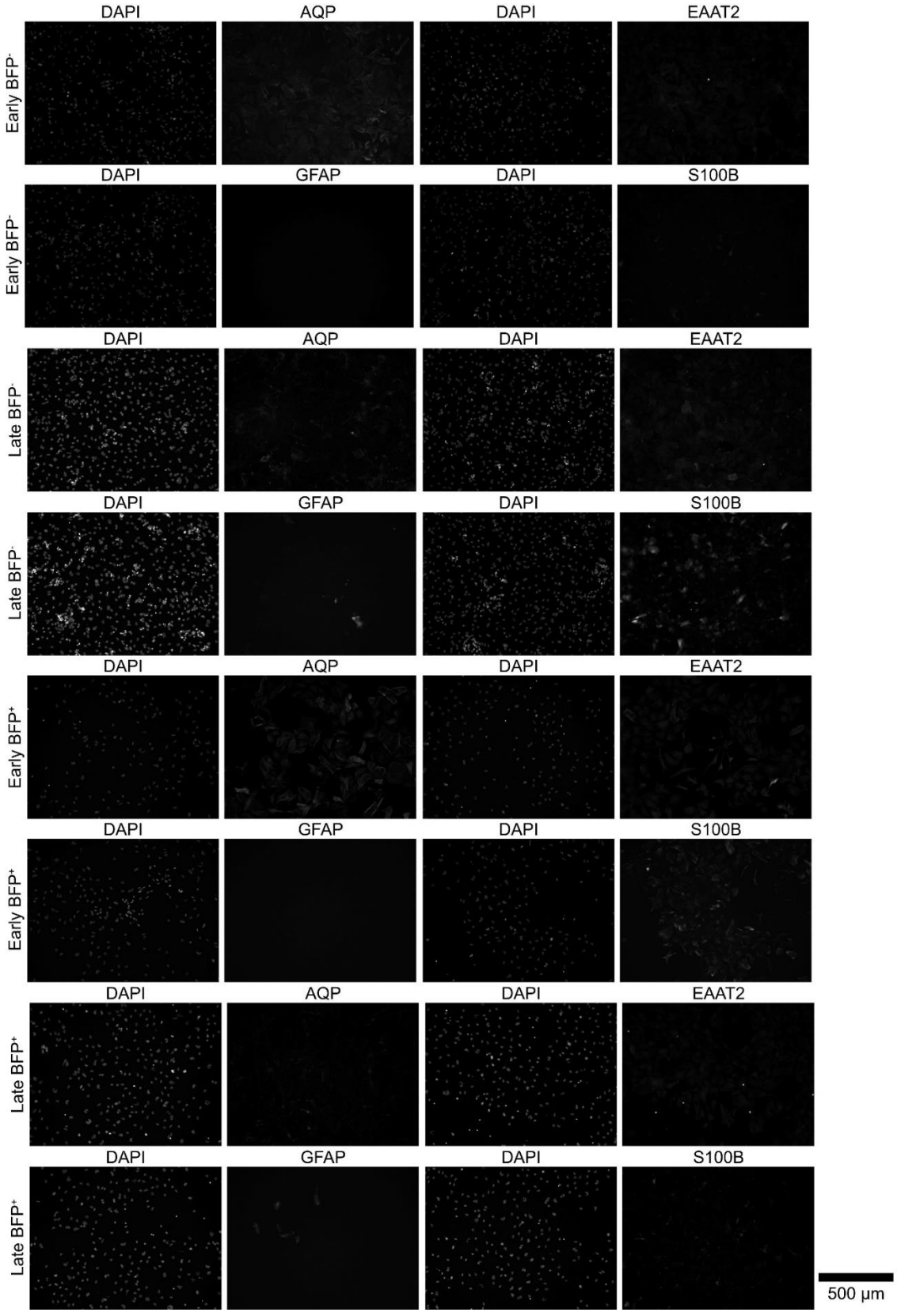

Figure S3. Original images of immunocytochemistry of astrocyte markers shown in Figure 2B.

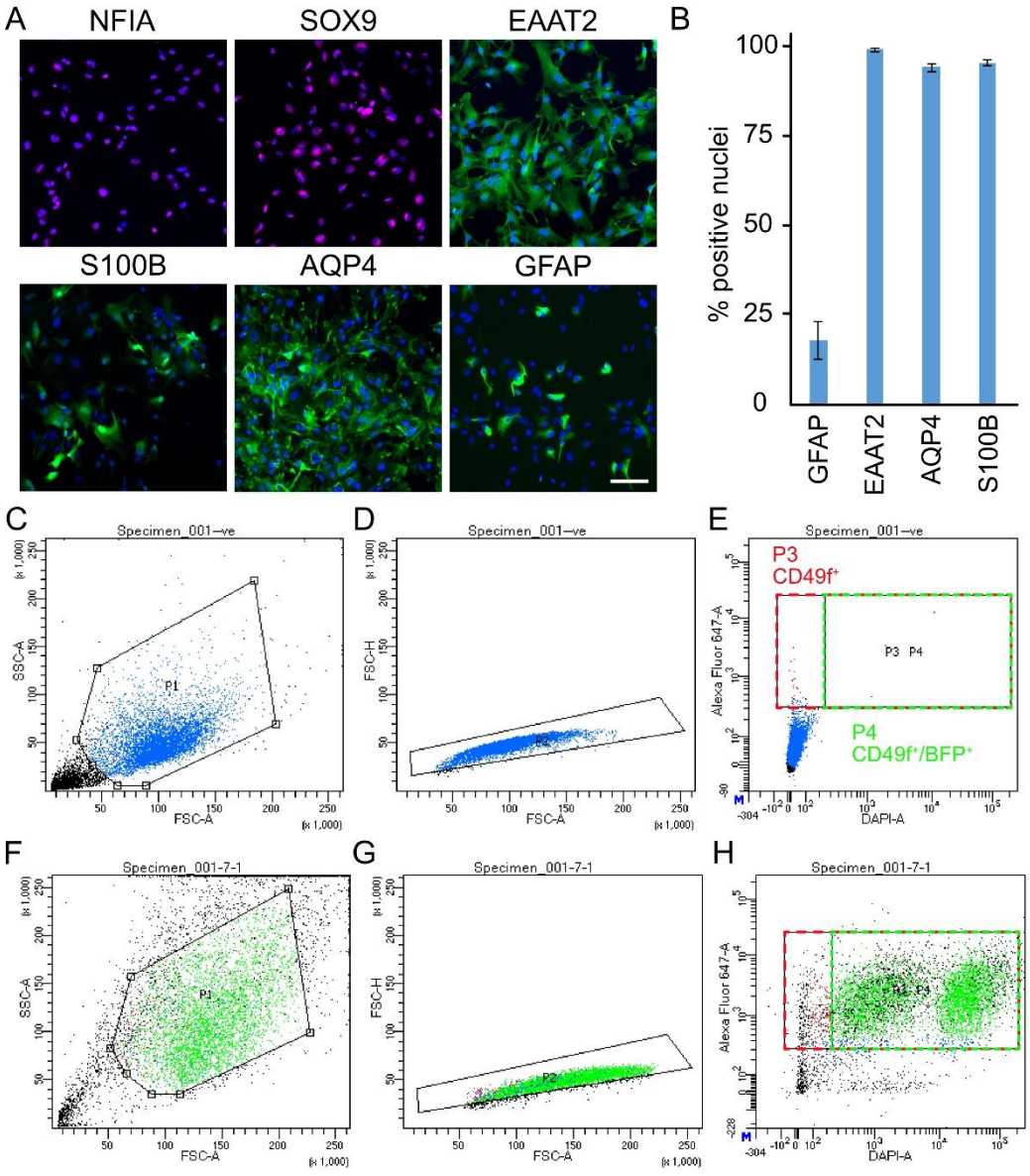

Figure S4. Non-patterned astrocytes and fluorescence-activated cell sorting of astrocytes for single cell RNA sequencing.

A, Representative view of immunocytochemistry of astrocyte marker expression in non-patterned astrocytes (scale bar represents 100 µm). B, Quantification of astrocyte marker expression in astrocytes. Error bars represent SEM of three independent experiments. C-E, negative control samples; F-H, one sample of BFP+ astrocytes). C and F shows the dot plot of SSC-A versus FSC-A. D and G shows the dot plot of FSC-H versus FSC-A. E and H shows the dot plot of Alexa Fluor-647-A (labelling CD49f) versus DAPI-A (labelling BFP). P3 was used to isolate $CD49f^+$ population (including both BFP^+ and BFP^-), while P4 was used to isolate $CD49f^+/BFP^+$ population.

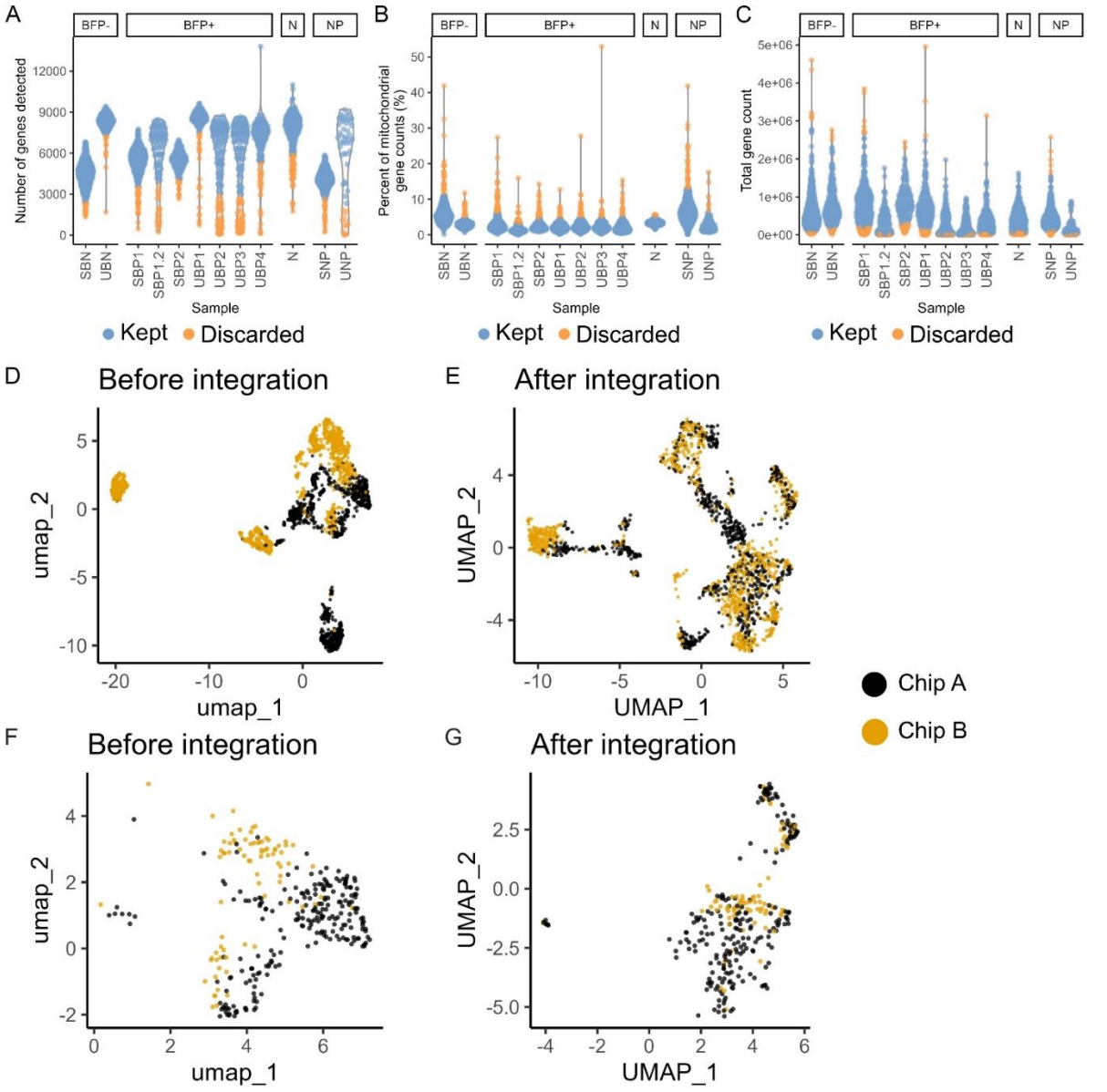

591

592 **Figure S5. Processing of single cell RNA sequencing data.**

593 A-C, Violin plots showing the results of adaptive cell-level filtering based on the
594 number of genes detected per cell (A), percentage of mitochondrial gene counts per
595 cell (B), and total gene count per cell (C). D-E, UMAP plot of all filtered cells before
596 (D) and after integration (E) coloured by chip. F-G, UMAP plot of the subset of sorted
597 BFP$^+$ astrocytes on Chip A and B derived from the same astrocyte differentiation
598 before (F) and after integration (G) coloured by chip. (N: neuron; SBN: sorted BFP$^-$;
599 SBP: sorted BFP$^+$; SNP: sorted non-patterned; UBN: unsorted BFP$^-$; UBP: unsorted
600 BFP$^+$; UNP: unsorted non-patterned; numbers represent independent samples)

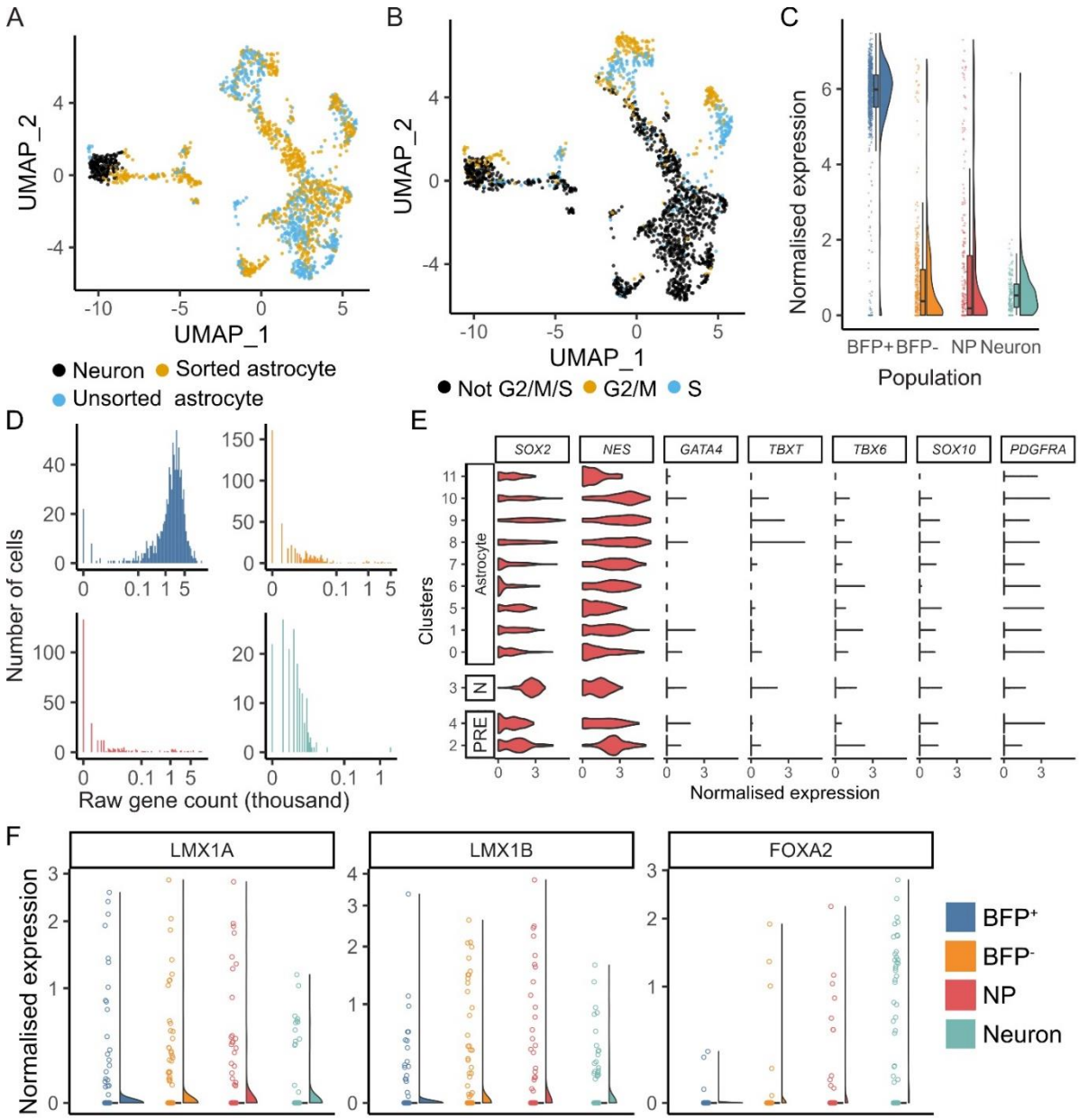

Figure S6. Marker expression in scRNAseq.

A-B, UMAP plot of all filtered cells after integration coloured by sample type and sorting status (A) and estimated cell cycle phase (B). C, Raincloud plots of normalised expression of *BFP*. D, Histogram of the distribution of raw gene count of *BFP*. E, Violin plots of the normalised expression of endoderm, mesoderm, neuroectoderm, and oligodendrocyte progenitor markers. F, Violin plots of the normalised expression of classic ventral midbrain markers.

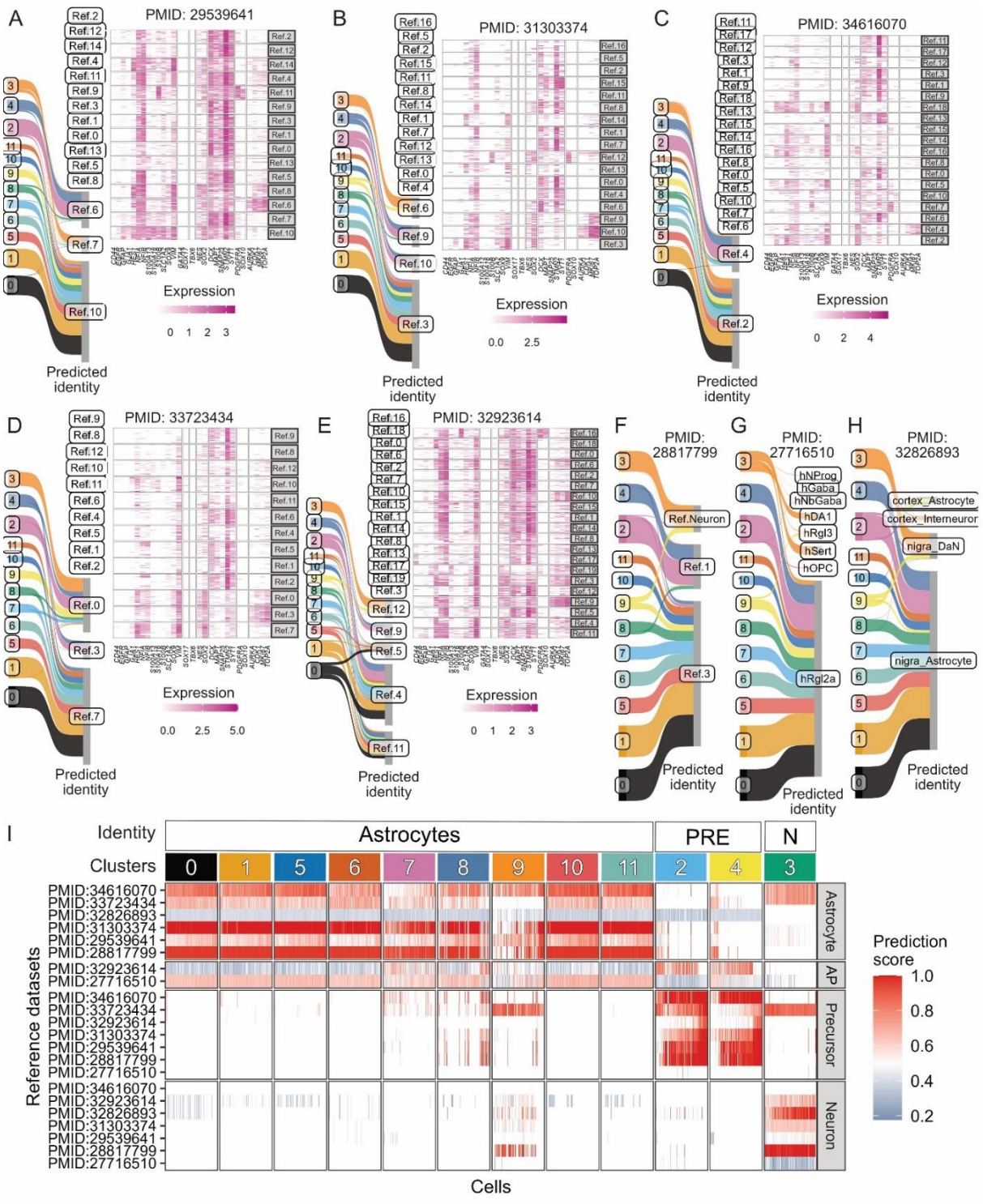

Figure S7. Reference mapping to human brain single cell RNA sequencing datasets.

A-H, Sankey plot summarising the result of reference mapping of cells in different clusters to eight published reference human brain scRNAseq datasets. The thickness of the thread is proportional to the number of cells mapped to the same identity in the

615 reference datasets (predicted identity). Cluster IDs in this study are shown on the left.
616 Heatmap in Panel A-E shows the expression of marker genes in different clusters in
617 the re-annotated reference datasets. I, Heatmap of prediction score from Seurat
618 integration.
619

620 **Supplementary Table 1. Antibodies used in this study.**

Target	Species	Producer	Catalogue number	Dilution for use
ALDH1L1	MS	Abcam	ab56777	1:500
AQP4	RB	Abcam	ab259318	1:200
BFP	rabbit	Evrogen	AB233	1:3000
CD44	mouse	Cell Signalling Technology	3750	1:400
EAAT2	goat	Abcam	ab235202	1:200
FOXA2	goat	R&D system	AF2400	1:1000
GFAP	rat	Life Tech	AB10533	1:1000
LMX1A	rabbit	Millipore	HPA030088	1:2000
NESTIN	mouse	BD	BD611659	1:300
NFIA	rabbit	Abcam	AB228897	1:1000
NKX6.1	mouse	DSHB	F55A10	1:100
OTX2	goat	R&D system	AF1979	1:200
PAX6	mouse	DSHB	PAX6	1:1000
S100B	rabbit	Abcam	ab52642	1:1000
SOX9	goat	R&D system	AF3075	1:300
Anti-Goat IgG, Alexa Fluor 488	donkey	Invitrogen	A32814	1:1000
Anti-Goat IgG, Alexa Fluor 555	donkey	Invitrogen	A32816	1:1000
Anti-Goat IgG, Alexa Fluor 647	donkey	Invitrogen	A32849	1:1000

Anti-Mouse IgG, Alexa Fluor 488	donkey	Invitrogen	A21202	1:1000
Anti-Mouse IgG, Alexa Fluor 555	donkey	Invitrogen	A31570	1:1000
Anti-Mouse IgG, Alexa Fluor 647	donkey	Invitrogen	A31571	1:1000
Anti-Rabbit IgG, Alexa Fluor 488	donkey	Invitrogen	A21206	1:1000
Anti-Rabbit IgG, Alexa Fluor 555	donkey	Invitrogen	A31572	1:1000
Anti-Rabbit IgG, Alexa Fluor 647	donkey	Invitrogen	A31573	1:1000
Anti-Rat IgG, Alexa Fluor 488	donkey	Invitrogen	A21208	1:1000

Supplementary Table 2. Settings used for processing published datasets.

PMID	Tissue	Age	Scale factor	PCs used	Harmony integration	Clustering resolution	Re-annotation
32826893	SN and cortex	Adult	10000	50	No	0.5	No
33723434	multiple	CS22	10000	50	Yes	0.3	Yes
34616070	multiple	GW25	10000	50	Yes	0.4	Yes
32923614	Neocortex	GW9-28	100000	30	Yes	0.9	Yes
31303374	Neocortex	GW17-18	10000	30	Yes	0.5	Yes
29539641	Prefrontal cortex	GW8-26	100000	30	Yes	0.9	Yes
28817799	PSC-derived astrocytes	-	10000	30	No	0.3	No
27716510	Ventral midbrain	GW7-11	10000	30	No	0.5	No

Supplementary Data 1: Pairwise DEGs of three astrocyte and one neuron populations.

Supplementary Data 2: GO enrichment of population enriched DEGs.

626 Supplementary Data 3: Representative enriched GO terms of DEGs for BFP+ and
627 BFP- astrocytes.

628 Supplementary Data 4: DEGs comparing sorted and unsorted populations.

629 Acknowledgements

630 We would like to thank Mark Bishop and Joanne Morgan for conducting FACS and
631 next generation sequencing, respectively. We thank Kathryn Peall and Laura Abram
632 for providing iPSC-derived neurons for scRNAseq. We also thank the support of the
633 Supercomputing Wales project, which is part-funded by the European Regional
634 Development Fund (ERDF) via the Welsh Government.

635 Author Contribution

636 Z.L. and M.L. conceived the study and designed the experiments. Z.L. performed all
637 cell experiments and analysed all data. L.C. and M.L. designed the lineage tracing
638 system, and L.C. generated the cell line with assistance from Z.L. M.R. performed
639 iCELL8 library preparation. J.M.S., F.W., and V.V. provided guidance and contributed
640 to general discussions on scRNAseq data analysis. C.W. contributed to the design of
641 scRNAseq and general discussions throughout the work. Z.L. and M.L wrote the
642 paper. All authors edited and approved the paper.

643 Funding

644 This work was supported by the UK Dementia Research Institute, jointly funded by the
645 UK Medical Research Council, Alzheimer's Society and Alzheimer's Research UK, to
646 C.W. (MC_PC_17112) and Z.L. (DRI-TRA2021-02), and a seed corn fund to Z.L. from
647 the Neuroscience and Mental Health Innovation Institute, Cardiff University. Z.L. was
648 funded by a UK Dementia Research Institute PhD studentship.

Data Availability

The sequencing data discussed in this publication have been deposited in NCBI's Gene Expression Omnibus (Clough and Barrett 2016) and are accessible through a GEO Series accession number which will be made available upon final publication.

Declaration of interests

The authors declare no competing interests.

References

Agarwal, D. et al. 2020. A single-cell atlas of the human substantia nigra reveals cell-specific pathways associated with neurological disorders. *Nat Commun* 11(1), p. 4183. doi: 10.1038/s41467-020-17876-0

Ahmed, M., Owens, M. J. S., Toledo, E. M., Arenas, E., Bradley, M. and Ffrench-Constant, C. 2021. Combinatorial ECM Arrays Identify Cooperative Roles for Matricellular Proteins in Enhancing the Generation of TH+ Neurons From Human Pluripotent Cells. *Front Cell Dev Biol* 9, p. 755406. doi: 10.3389/fcell.2021.755406

Andersson, E. et al. 2006. Identification of intrinsic determinants of midbrain dopamine neurons. *Cell* 124(2), pp. 393-405. doi: 10.1016/j.cell.2005.10.037

Barbar, L. et al. 2020. CD49f Is a Novel Marker of Functional and Reactive Human iPSC-Derived Astrocytes. *Neuron* 107(3), pp. 436-453 e412. doi: 10.1016/j.neuron.2020.05.014

Barbuti, P. A. et al. 2020. IPSC-derived midbrain astrocytes from Parkinson's disease patients carrying pathogenic SNCA mutations exhibit alpha-synuclein aggregation, mitochondrial fragmentation and excess calcium release. *bioRxiv*, p. 2020.2004.2027.053470. doi: 10.1101/2020.04.27.053470

677 Batiuk, M. Y. et al. 2020. Identification of region-specific astrocyte subtypes at single
678 cell resolution. *Nature Communications* 11(1), doi: 10.1038/s41467-019-14198-8

679

680 Bayraktar, O. A. et al. 2020. Astrocyte layers in the mammalian cerebral cortex
681 revealed by a single-cell in situ transcriptomic map. *Nature Neuroscience* 23(4), pp.
682 500-509. doi: 10.1038/s41593-020-0602-1

683

684 Bhaduri, A. et al. 2021. An atlas of cortical arealization identifies dynamic molecular
685 signatures. *Nature* 598(7879), pp. 200-204. doi: 10.1038/s41586-021-03910-8

686

687 Bifsha, P., Balsalobre, A. and Drouin, J. 2017. Specificity of Pitx3-Dependent Gene
688 Regulatory Networks in Subsets of Midbrain Dopamine Neurons. *Molecular*
689 *Neurobiology* 54(7), pp. 4921-4935. doi: 10.1007/s12035-016-0040-y

690

691 Booth, H. D. E., Hirst, W. D. and Wade-Martins, R. 2017. The Role of Astrocyte
692 Dysfunction in Parkinson's Disease Pathogenesis. *Trends in neurosciences* 40(6), pp.
693 358-370. doi: 10.1016/j.tins.2017.04.001

694

695 Booth, H. D. E. et al. 2019. RNA sequencing reveals MMP2 and TGFB1
696 downregulation in LRRK2 G2019S Parkinson's iPSC-derived astrocytes. *Neurobiol*
697 *Dis* 129, pp. 56-66. doi: 10.1016/j.nbd.2019.05.006

698

699 Bradley, R. A. et al. 2019. Regionally specified human pluripotent stem cell-derived
700 astrocytes exhibit different molecular signatures and functional properties.
701 *Development* 146(13), p. dev170910. doi: 10.1242/dev.170910

702

703 Cardo, L. F., Monzón-Sandoval, J., Li, Z., Webber, C. and Li, M. 2023. Single-Cell
704 Transcriptomics and In Vitro Lineage Tracing Reveals Differential Susceptibility of
705 Human iPSC-Derived Midbrain Dopaminergic Neurons in a Cellular Model of
706 Parkinson's Disease. *Cells* 12(24), doi: 10.3390/cells12242860

707

708 Carlson, M. 2019. org.Hs.eg.db: Genome wide annotation for Human. R package
709 version 3.8.2.

710

711 Chai, H. et al. 2017. Neural Circuit-Specialized Astrocytes: Transcriptomic, Proteomic,
712 Morphological, and Functional Evidence. *Neuron* 95(3), pp. 531-549 e539. doi:
713 10.1016/j.neuron.2017.06.029

714

715 Chandrasekaran, A., Avci, H. X., Leist, M., Kobolák, J. and Dinnyés, A. 2016.
716 Astrocyte Differentiation of Human Pluripotent Stem Cells: New Tools for Neurological
717 Disorder Research. *Frontiers in cellular neuroscience* 10, pp. 215-215. doi:
718 10.3389/fncel.2016.00215

719

720 Chung, N. C. and Storey, J. D. 2015. Statistical significance of variables driving
721 systematic variation in high-dimensional data. *Bioinformatics* 31(4), pp. 545-554. doi:
722 10.1093/bioinformatics/btu674

723

724 Clough, E. and Barrett, T. 2016. The Gene Expression Omnibus Database. *Methods*
725 *Mol Biol* 1418, pp. 93-110. doi: 10.1007/978-1-4939-3578-9_5

726

727 Crompton, L. A., McComish, S. F., Stathakos, P., Cordero-Llana, O., Lane, J. D. and
728 Caldwell, M. A. 2021. Efficient and Scalable Generation of Human Ventral Midbrain
729 Astrocytes from Human-Induced Pluripotent Stem Cells. *Journal of Visualized*
730 *Experiments* (176), doi: 10.3791/62095

731

732 Crompton, L. A., McComish, S. F., Steward, T. G. J., Whitcomb, D. J., Lane, J. D. and
733 Caldwell, M. A. 2023. Human stem cell-derived ventral midbrain astrocytes exhibit a
734 region-specific secretory profile. *Brain Commun* 5(2), p. fcad114. doi:
735 10.1093/braincomms/fcad114

736

737 de Rus Jacquet, A., Tancredi, J. L., Lemire, A. L., DeSantis, M. C., Li, W. P. and
738 O'Shea, E. K. 2021. The LRRK2 G2019S mutation alters astrocyte-to-neuron
739 communication via extracellular vesicles and induces neuron atrophy in a human
740 iPSC-derived model of Parkinson's disease. *Elife* 10, p. 2020.2007.2002.178574. doi:
741 10.7554/eLife.73062

742

743 Deneen, B., Ho, R., Lukaszewicz, A., Hochstim, C. J., Gronostajski, R. M. and
744 Anderson, D. J. 2006. The Transcription Factor NFIA Controls the Onset of
745 Gliogenesis in the Developing Spinal Cord. *Neuron* 52(6), pp. 953-968. doi:
746 10.1016/j.neuron.2006.11.019

747

748 di Domenico, A. et al. 2019. Patient-Specific iPSC-Derived Astrocytes Contribute to
749 Non-Cell-Autonomous Neurodegeneration in Parkinson's Disease. *Stem cell reports*
750 12(2), pp. 213-229. doi: 10.1016/j.stemcr.2018.12.011

751

752 Dobin, A. et al. 2013. STAR: ultrafast universal RNA-seq aligner. *Bioinformatics* 29(1),
753 pp. 15-21. doi: 10.1093/bioinformatics/bts635

754

755 Duan, D., Fu, Y., Paxinos, G. and Watson, C. 2013. Spatiotemporal expression
756 patterns of Pax6 in the brain of embryonic, newborn, and adult mice. *Brain Structure*
757 *and Function* 218(2), pp. 353-372. doi: 10.1007/s00429-012-0397-2

758

759 Endo, F. et al. 2022. Molecular basis of astrocyte diversity and morphology across the
760 CNS in health and disease. *Science* 378(6619), p. eadc9020. doi:
761 doi:10.1126/science.adc9020

762

763 Eze, U. C., Bhaduri, A., Haeussler, M., Nowakowski, T. J. and Kriegstein, A. R. 2021.
764 Single-cell atlas of early human brain development highlights heterogeneity of human
765 neuroepithelial cells and early radial glia. *Nature Neuroscience* 24(4), pp. 584-594.
766 doi: 10.1038/s41593-020-00794-1

767

768 Falk, A. et al. 2012. Capture of neuroepithelial-like stem cells from pluripotent stem
769 cells provides a versatile system for in vitro production of human neurons. *PLOS ONE*
770 7(1), p. e29597. doi: 10.1371/journal.pone.0029597

771

772 Fan, X. et al. 2020. Single-cell transcriptome analysis reveals cell lineage specification
773 in temporal-spatial patterns in human cortical development. *Science Advances* 6(34),
774 p. eaaz2978. doi: doi:10.1126/sciadv.aaz2978

775

776 Finak, G. et al. 2015. MAST: a flexible statistical framework for assessing
777 transcriptional changes and characterizing heterogeneity in single-cell RNA
778 sequencing data. *Genome Biology* 16(1), p. 278. doi: 10.1186/s13059-015-0844-5

779

780 Gabay, L., Lowell, S., Rubin, L. L. and Anderson, D. J. 2003. Deregulation of
781 dorsoventral patterning by FGF confers trilineage differentiation capacity on CNS stem
782 cells in vitro. *Neuron* 40(3), pp. 485-499. doi: 10.1016/s0896-6273(03)00637-8

783

784 Hedegaard, A., Monzón-Sandoval, J., Newey, S. E., Whiteley, E. S., Webber, C. and
785 Akerman, C. J. 2020. Pro-maturational Effects of Human iPSC-Derived Cortical
786 Astrocytes upon iPSC-Derived Cortical Neurons. *Stem cell reports* 15(1), pp. 38-51.
787 doi: https://doi.org/10.1016/j.stemcr.2020.05.003

788

789 Holmqvist, S. et al. 2015. Generation of human pluripotent stem cell reporter lines for
790 the isolation of and reporting on astrocytes generated from ventral midbrain and
791 ventral spinal cord neural progenitors. *Stem Cell Research* 15(1), pp. 203-220. doi:
792 https://doi.org/10.1016/j.scr.2015.05.014

793

794 Houweling, A. C., Dildrop, R., Peters, T., Mummenhoff, J., Moorman, A. F. M., Rüther,
795 U. and Christoffels, V. M. 2001. Gene and cluster-specific expression of the Iroquois
796 family members during mouse development. *Mechanisms of Development* 107(1), pp.
797 169-174. doi: https://doi.org/10.1016/S0925-4773(01)00451-8

798

799 Itoh, N. et al. 2018. Cell-specific and region-specific transcriptomics in the multiple
800 sclerosis model: Focus on astrocytes. *Proceedings of the National Academy of*
801 *Sciences* 115(2), pp. E302-E309. doi: doi:10.1073/pnas.1716032115

802

803 Jaeger, I. et al. 2011. Temporally controlled modulation of FGF/ERK signaling directs
804 midbrain dopaminergic neural progenitor fate in mouse and human pluripotent stem
805 cells. *Development* 138(20), pp. 4363-4374. doi: 10.1242/dev.066746

806

807 Jain, M., Armstrong, R. J., Tyers, P., Barker, R. A. and Rosser, A. E. 2003. GABAergic
808 immunoreactivity is predominant in neurons derived from expanded human neural
809 precursor cells in vitro. *Exp Neurol* 182(1), pp. 113-123. doi: 10.1016/s0014-
810 4886(03)00055-4

811

812 Kamath, T. et al. 2022. Single-cell genomic profiling of human dopamine neurons
813 identifies a population that selectively degenerates in Parkinson's disease. *Nature*
814 *Neuroscience* 25(5), pp. 588-595. doi: 10.1038/s41593-022-01061-1

815

816 Koch, P., Opitz, T., Steinbeck, J. A., Ladewig, J. and Brüstle, O. 2009. A rosette-type,
817 self-renewing human ES cell-derived neural stem cell with potential for in vitro
818 instruction and synaptic integration. *Proc Natl Acad Sci U S A* 106(9), pp. 3225-3230.
819 doi: 10.1073/pnas.0808387106

820

821 Kostuk, E. W., Cai, J. and Iacovitti, L. 2019. Subregional differences in astrocytes
822 underlie selective neurodegeneration or protection in Parkinson's disease models in
823 culture. *Glia* 67(8), pp. 1542-1557. doi: 10.1002/glia.23627

824

825 Krencik, R., Weick, J. P., Liu, Y., Zhang, Z.-J. and Zhang, S.-C. 2011. Specification of
826 transplantable astroglial subtypes from human pluripotent stem cells. *Nature*
827 *Biotechnology* 29, p. 528. doi: 10.1038/nbt.1877

828 https://www.nature.com/articles/nbt.1877#supplementary-information

829

830 La Manno, G. et al. 2016. Molecular Diversity of Midbrain Development in Mouse,
831 Human, and Stem Cells. *Cell* 167(2), pp. 566-580.e519. doi:
832 10.1016/j.cell.2016.09.027

833

834 Li, Y. et al. 2023. Spatiotemporal transcriptome atlas reveals the regional specification
835 of the developing human brain. *Cell* 186(26), pp. 5892-5909.e5822. doi:
836 https://doi.org/10.1016/j.cell.2023.11.016

837

838 Liao, Y., Smyth, G. K. and Shi, W. 2013. The Subread aligner: fast, accurate and
839 scalable read mapping by seed-and-vote. *Nucleic Acids Res* 41(10), p. e108. doi:
840 10.1093/nar/gkt214

841

842 Lin, Y.-T. et al. 2018. APOE4 Causes Widespread Molecular and Cellular Alterations
843 Associated with Alzheimer's Disease Phenotypes in Human iPSC-Derived Brain Cell
844 Types. *Neuron* 98(6), pp. 1141-1154.e1147. doi:
845 https://doi.org/10.1016/j.neuron.2018.05.008

846

847 Liu, Y. et al. 2004. CD44 expression identifies astrocyte-restricted precursor cells.
848 *Developmental Biology* 276(1), pp. 31-46. doi:
849 https://doi.org/10.1016/j.ydbio.2004.08.018

850

Lozzi, B., Huang, T. W., Sardar, D., Huang, A. Y. S. and Deneen, B. 2020. Regionally Distinct Astrocytes Display Unique Transcription Factor Profiles in the Adult Brain. *Frontiers in Neuroscience* 14, doi: 10.3389/fnins.2020.00061

Makarava, N., Chang, J. C.-Y., Kushwaha, R. and Baskakov, I. V. 2019. Region-Specific Response of Astrocytes to Prion Infection. *Frontiers in Neuroscience* 13, doi: 10.3389/fnins.2019.01048

Matsunaga, E., Araki, I. and Nakamura, H. 2001. Role of Pax3/7 in the tectum regionalization. *Development* 128(20), pp. 4069-4077. doi: 10.1242/dev.128.20.4069

McCarthy, D. J., Campbell, K. R., Lun, A. T. L. and Wills, Q. F. 2017. Scater: pre-processing, quality control, normalization and visualization of single-cell RNA-seq data in R. *Bioinformatics* 33(8), pp. 1179-1186. doi: 10.1093/bioinformatics/btw777

Molofsky, A. V. et al. 2012. Astrocytes and disease: a neurodevelopmental perspective. *Genes & Development* 26(9), pp. 891-907. doi: 10.1101/gad.188326.112

Morel, L. et al. 2017. Molecular and Functional Properties of Regional Astrocytes in the Adult Brain. *J Neurosci* 37(36), pp. 8706-8717. doi: 10.1523/JNEUROSCI.3956-16.2017

Nolbrant, S., Heuer, A., Parmar, M. and Kirkeby, A. 2017. Generation of high-purity human ventral midbrain dopaminergic progenitors for in vitro maturation and intracerebral transplantation. *Nature Protocols* 12(9), pp. 1962-1979. doi: 10.1038/nprot.2017.078

Oberheim, N. A. et al. 2009. Uniquely hominid features of adult human astrocytes. *J Neurosci* 29(10), pp. 3276-3287. doi: 10.1523/jneurosci.4707-08.2009

Peteri, U.-K., Pitkonen, J., Utami, K. H., Paavola, J., Roybon, L., Pouladi, M. A. and Castrén, M. L. 2021. Generation of the Human Pluripotent Stem-Cell-Derived Astrocyte Model with Forebrain Identity. *Brain sciences* 11(2), p. 209. doi: 10.3390/brainsci11020209

Phatnani, H. and Maniatis, T. 2015. Astrocytes in neurodegenerative disease. *Cold Spring Harbor perspectives in biology* 7(6), p. a020628. doi: 10.1101/cshperspect.a020628

Polioudakis, D. et al. 2019. A Single-Cell Transcriptomic Atlas of Human Neocortical Development during Mid-gestation. *Neuron* 103(5), pp. 785-801.e788. doi: 10.1016/j.neuron.2019.06.011

Roybon, L. et al. 2013. Human stem cell-derived spinal cord astrocytes with defined mature or reactive phenotypes. *Cell Rep* 4(5), pp. 1035-1048. doi: 10.1016/j.celrep.2013.06.021

Schindelin, J. et al. 2012. Fiji: an open-source platform for biological-image analysis. *Nature Methods* 9(7), pp. 676-682. doi: 10.1038/nmeth.2019

Schlicker, A., Domingues, F. S., Rahnenführer, J. and Lengauer, T. 2006. A new measure for functional similarity of gene products based on Gene Ontology. *BMC Bioinformatics* 7(1), p. 302. doi: 10.1186/1471-2105-7-302

Schober, A. L., Wicki-Stordeur, L. E., Murai, K. K. and Swayne, L. A. 2022. Foundations and implications of astrocyte heterogeneity during brain development and disease. *Trends in neurosciences* 45(9), pp. 692-703. doi: 10.1016/j.tins.2022.06.009

Serio, A. et al. 2013. Astrocyte pathology and the absence of non-cell autonomy in an induced pluripotent stem cell model of TDP-43 proteinopathy. *Proceedings of the National Academy of Sciences of the United States of America* 110(12), pp. 4697-4702. doi: 10.1073/pnas.1300398110

Sloan, S. A. et al. 2017. Human Astrocyte Maturation Captured in 3D Cerebral Cortical Spheroids Derived from Pluripotent Stem Cells. *Neuron* 95(4), pp. 779-790 e776. doi: 10.1016/j.neuron.2017.07.035

Sonninen, T.-M. et al. 2020. Metabolic alterations in Parkinson's disease astrocytes. *Scientific Reports* 10(1), p. 14474. doi: 10.1038/s41598-020-71329-8

Stirling, D. R., Swain-Bowden, M. J., Lucas, A. M., Carpenter, A. E., Cimini, B. A. and Goodman, A. 2021. CellProfiler 4: improvements in speed, utility and usability. *BMC Bioinformatics* 22(1), p. 433. doi: 10.1186/s12859-021-04344-9

Stolt, C. C., Lommes, P., Sock, E., Chaboissier, M.-C., Schedl, A. and Wegner, M. 2003. The Sox9 transcription factor determines glial fate choice in the developing spinal cord. *Genes & Development* 17(13), pp. 1677-1689. doi: 10.1101/gad.259003

Strelau, J. et al. 2000. Growth/differentiation factor-15/macrophage inhibitory cytokine-1 is a novel trophic factor for midbrain dopaminergic neurons in vivo. *J Neurosci* 20(23), pp. 8597-8603. doi: 10.1523/jneurosci.20-23-08597.2000

Stuart, T. et al. 2019. Comprehensive Integration of Single-Cell Data. *Cell* 177(7), pp. 1888-1902.e1821. doi: 10.1016/j.cell.2019.05.031

Sun, Y. et al. 2008. Long-term tripotent differentiation capacity of human neural stem (NS) cells in adherent culture. *Mol Cell Neurosci* 38(2), pp. 245-258. doi: 10.1016/j.mcn.2008.02.014

Supek, F., Bošnjak, M., Škunca, N. and Šmuc, T. 2011. REVIGO Summarizes and Visualizes Long Lists of Gene Ontology Terms. *PLOS ONE* 6(7), p. e21800. doi: 10.1371/journal.pone.0021800

Takata, N. and Hirase, H. 2008. Cortical Layer 1 and Layer 2/3 Astrocytes Exhibit Distinct Calcium Dynamics In Vivo. *PLOS ONE* 3(6), p. e2525. doi: 10.1371/journal.pone.0002525

Tcw, J. et al. 2017. An Efficient Platform for Astrocyte Differentiation from Human Induced Pluripotent Stem Cells. *Stem cell reports* 9(2), pp. 600-614. doi: 10.1016/j.stemcr.2017.06.018

953 Team, R. C. 2023. : A Language and Environment for Statistical Computing. Vienna,
954 Austria: R Foundation for Statistical Computing, .

955

956 Verkhratsky, A. and Nedergaard, M. 2018. Physiology of astroglia. *Physiological*
957 *Reviews* 98(1), pp. 239-389. doi: 10.1152/physrev.00042.2016

958

959 Xin, W., Schuebel, K. E., Jair, K.-w., Cimbro, R., De Biase, L. M., Goldman, D. and
960 Bonci, A. 2019. Ventral midbrain astrocytes display unique physiological features and
961 sensitivity to dopamine D2 receptor signaling. *Neuropsychopharmacology* 44(2), pp.
962 344-355. doi: 10.1038/s41386-018-0151-4

963

964 Yun, W. et al. 2019. Generation of Anterior Hindbrain-Specific, Glial-Restricted
965 Progenitor-Like Cells from Human Pluripotent Stem Cells. *Stem Cells and*
966 *Development* 28(10), pp. 633-648. doi: 10.1089/scd.2019.0033

967

968 Zhong, S. et al. 2018. A single-cell RNA-seq survey of the developmental landscape
969 of the human prefrontal cortex. *Nature* 555(7697), pp. 524-528. doi:
970 10.1038/nature25980

971

972 Zhou, S. et al. 2016. Neurosphere Based Differentiation of Human iPSC Improves
973 Astrocyte Differentiation. *Stem Cells Int* 2016, p. 4937689. doi: 10.1155/2016/4937689

974

975 Zhu, Q., Shah, S., Dries, R., Cai, L. and Yuan, G. C. 2018. Identification of spatially
976 associated subpopulations by combining scRNAseq and sequential fluorescence in
977 situ hybridization data. *Nat Biotechnol* 36(12), pp. 1183-1190. doi: 10.1038/nbt.4260

978

979